Genesis of the Tangshang Au Deposit in Southeast Yunnan Province, China: Constraints from In Situ Chemical and S-Sr Isotope Analyses

Weifang Song [1], Pan Wu [1,2,*], Jianzhong Liu [1,3,4,*], Junhai Li [5], Zepeng Wang [5], Qinping Tan [6], Zhuojun Xie [6] and Lulin Zheng [7]

1   College of Resource and Environmental Engineering, Guizhou University, Guiyang 550025, China; gs.wfsong19@gzu.edu.cn
2   Key Laboratory of Karst Geological Resources and Environment, Ministry of Education of the People's Republic of China, Guiyang 550025, China
3   Guizhou Bureau of Geology and Mineral Exploration & Development, Guiyang 550004, China
4   Innovation Center Ore Resources Exploration Technology in the Region of Bedrock, Ministry of Natural Resources of the People's Republic of China, Guiyang 550018, China
5   Geological Party 105 of the Guizhou Bureau of Geology and Mineral Exploration & Development, Guiyang 550018, China; lijunhai2020@163.com (J.L.); wangzepengyu@126.com (Z.W.)
6   State Key Laboratory of Ore Deposit Geochemistry, Institute of Geochemistry, Chinese Academy of Sciences, Guiyang 550081, China; tanqinping@vip.gyig.ac.cn (Q.T.); xiezhuojun@vip.gyig.ac.cn (Z.X.)
7   College of Mining, Guizhou University, Guiyang 550025, China; llzheng@gzu.edu.cn
*   Correspondence: pwu@gzu.edu.cn (P.W.); ljz13765115603@163.com (J.L.)

Abstract: The Yunnan–Guizhou–Guangxi district (also known as the Dian–Qian–Gui "Golden Triangle") in southwestern China contains numerous Carlin-type Au deposits (CTGDs). However, the sources of Au and Au-bearing fluids in these deposits remain controversial. The Tangshang Au deposit is a middle-sized CTGD in southeastern Yunnan Province. This study involved in situ chemical and S isotope analyses of sulfides and in situ trace elemental and Sr isotope analyses of ore-related calcite; these data were used to trace the sources of fluids and Au, as well as the genesis of this deposit. Four pyrite types (Py1, Py2, Py3, and Py4) and two arsenopyrite types (Apy1 and Apy2) were identified based on their textural characteristics. It was found that Py1 contains relatively lower Au, Sb, Cu, and Tl contents than those of Py2, Py3, and Py4. Py1 is wrapped by rim-Py2 and Py3, which indicates an early-ore-stage genesis. The Carlin-type mineralization elements are elevated in the pyrites (Au = 3.04–38.1 ppm; As = 40,932–65,833 ppm; Tl = 0 to 3.3 ppm; Sb = 1.2 to 343 ppm; and Cu = 10 to 102 ppm), and the average Co/Ni ratio is 0.54. Additionally, Au has a positive correlation with Tl and Cu. The high concentrations of As and Au in all types of pyrite indicate that the ore-forming fluids are rich in both elements. The sulfides in the ores were shown to produce similar S isotope ratios, which are obviously higher than the S isotope value of sulfide (~0‰) in Emeishan basalt; therefore, the integration of these and elemental composition data indicated that all pyrites (Py1, Py2, Py3, and Py4) form during the ore stage. These results also demonstrate that the δ^{34}S values of the Au-bearing fluids are higher than those of basalt wall rocks. The flat chondrite-normalized REEs pattern and positive Eu anomaly of the calcite were similar to those obtained from Emeishan basalt, which suggests a reducing characteristic of hydrothermal fluids. The ^{87}Sr/^{86}Sr ratios (0.70557–0.70622) of calcite were also comparable to the range obtained from Emeishan basalt. Some slightly higher ^{87}Sr/^{86}Sr ratios, which ranged between those obtained from Emeishan basalt and limestone from the Maokou Formation, indicated that the Sr isotope ratios of the Au-bearing fluids are higher than those of Emeishan basalt. Based on data generated in the present study and the regional geology of this area, a genetic model involving a metamorphic fluid system was proposed for the Tangshang gold deposit, and a gold mineralization event related to metamorphic fluid in the south of the Dian–Qian–Gui "Golden Triangle" was indicated.

Keywords: gold-bearing sulfides; calcite; in situ analysis; trace elements; S-Sr isotopes; Tangshang gold deposit

1. Introduction

Carlin-type gold deposits (CTGDs) are major sources of the gold (Au) mined worldwide [1–4]. Prominent CTGDs are found in Nevada (USA) and in the two "Golden Triangles" of Yunnan–Guizhou–Guangxi (Dian–Qian–Gui) and Shanxi–Gansu–Sichuan (Shan–Gan–Chuan) in southwestern China [5–18]. Carlin-type deposits in the northern Dian–Qian–Gui district are present in Permian to Triassic period platform carbonate, and they are also present in calcareous clastic rocks in the Dian–Qian–Gui area located in the southwest margin of the Yangtze Craton. Several gold deposits in the southern Dian–Qian–Gui "Golden Triangle" are present in Cambrian to Triassic calcareous clastic rocks and in Late Permian local diabase intrusions and volcaniclastic rocks [13]. Although several gold deposits are strata-bound, lots of ore deposits are localized by compressive shear zones [13]. Predecessors have summarized the characteristics of sediment-hosted ore deposits in the "Golden Triangles" [7]. The gold deposits have features similar to typical Carlin-type gold deposits in Nevada, USA, and are notably enriched in Sb, As, Hg, and Tl. Au occurs invisibly as a solid solution with submicrometer-sized particles in As-rich rim-pyrite and arsenopyrite [7,13,17]. Stibnite, orpiment, and realgar in the late-ore stage fill fractures on the periphery of gold mineralization [13]. The process of Carlin-type gold mineralization is fairly well described. The main mechanism controlling gold precipitation is considered to be sulfidation, whereby Au and sulfides (pyrite and arsenopyrite) precipitate together from Fe-poor, H_2S-rich, weakly acidic, and reductive fluids that react with Fe-carrying minerals in the host rocks. Southeastern Yunnan Province is an important area for Au occurrence within the Yunnan–Guizhou–Guangxi "Golden Triangle." Following the discovery of the Banqi deposit in southwestern Guizhou Province [19], dozens of other CTGDs have been discovered in the area [20]. The principal deposits among these are the Tangshang [20,21], Laozhaiwan [22], Zhesang [23], and Gedang deposits [24]. Even though the Tangshang deposit is known as the largest Au deposit in southeastern Yunnan Province, its genesis remains unclear. Therefore, investigations on the genesis of this deposit are necessary to improve the understanding of the associated Au mineralization and metallogenic system in the area. The main proposals regarding the origin of hydrothermal fluids rich in Au in the area include: (1) interaction with existing strata containing high concentrations of Au [16,25]; (2) the extraction of Au from sedimentary strata via metamorphic fluids [13,26]; and (3) the supply of Au from deep-seated magmatic intrusions [8,9,27–29].

Pyrite and arsenopyrite are common Au-carrying sulfides in CTGDs [14,30–32]. Therefore, to determine the genesis of such deposits, elemental and S isotope analyses of sulfides are valuable. In addition, elemental and isotope analyses of Sr in hydrothermally altered carbonates associated with Au-bearing sulfides can facilitate the understanding of the genesis of these orebodies. However, the composition of pyrite can vary significantly because it can be formed in diverse environments, including sedimentary, magmatic, and metamorphic conditions. In addition, because of the structural complexity and fine particle size of the Au-bearing sulfides in Carlin-type deposits, the determination of the genesis of pyrite through elemental analyses is challenging [3,7,11,12,17,26,29,30,33]. Moreover, traditional chemical analyses on a mineral or ores are inadequate for unraveling the genesis of sulfides and carbonate minerals associated with hydrothermal fluids because of significant variations in data. Such limitations restrict our understanding of the genesis of these deposits. However, recent advances in analytical technology can enable the in situ determination of the compositions of minerals associated with hydrothermal events. These measurements are significant for unraveling the genesis of these deposits [7,29,32–38].

The Tangshang Au deposit is reported to contain approximately 16 tons of Au, with an average grade of 1.45 g/t [39]. However, we still lack detailed studies on this deposit because of the impact of pervasive oxidation and the weathering of the orebodies; previous studies have only reported on a few trace elements in the ores and S isotope data of single minerals [20,21,39]. Recently, several small primary Au orebodies were discovered in the Emeishan basalt, which enabled the collection of samples for the direct investigation of the genesis of this deposit. In the present study, we used advanced and reliable in situ analysis

technology to study the main Au-bearing sulfides (pyrite and arsenopyrite) and gangue mineral hydrothermal calcite in the ores to more accurately determine the genesis of the gold deposit. On the basis of this study, a genetic model involving a metamorphic fluid is proposed for the Tangshang Au deposit. This study is of great value for understanding the genesis of gold deposits in the Yunnan–Guizhou–Guangxi district.

2. Geological Background

2.1. Regional Geology

The South China Block in the southeast of Eurasia comprises the Cathaysia Block and Yangtze Block, and it is bound by the Indo-China Block in the west and the North China Craton in the north [4]. The Song Ma and Qinling–Dabie suture zones in the west and north, respectively, formed because of a continental collision in the Triassic period [40–43] (Figure 1). The Dian–Qian–Gui "Golden Triangle," which is at the intersection of the Cathaysian Block and Yangtze Craton (Figure 1), is among the most important areas hosting CTGDs in China [44], and it characterized by two tectono-sedimentary units. Calcareous clastic rocks interbedded with carbonates formed in shallow-water platforms, and these are scattered across the northwest of the Triassic Youjiang Basin. According to Wang et al., deep water facies include turbidite sequences in the southeast of the Youjiang Basin [45] (Figure 1). Activities linked to the Yanshanian regional tectonic event alternated, which led to extension after the subduction of the continental plate, plate rifting, and magmatic intrusion. These activities significantly controlled the formation of CTGDs in the region [46]. Prominent structures in the study area include groups of deep major faults extending across the region and major folds involving anticlinal cores that are favorable locations for CTGDs, even though distinct strata-bound features are evident in each mining area [47]. Neoarchean to Neoproterozoic metamorphic rocks and calcareous clastic and carbonate rocks of Cambrian to Triassic ages are exposed in the area [20,21,39]. The main magmatic activities in the "Golden Triangle" produced Emeishan basalt in the Late Permian [48], quartz porphyry dykes in the Early Cretaceous [49], and lamprophyre dykes in the Late Cretaceous [50], as depicted in Figure 1.

Metallogenic ages of 275–46 Ma have been reported for the CTGDs in the "Golden Triangle", and these ages can be grouped into two periods: Late Triassic (240–200 Ma) and Late Jurassic to Early Cretaceous (148–134 Ma) [17,23,50–56]. Consequently, some studies suggest that the CTGDs in the area are associated with distinct mineralization events that occurred in the Late Triassic and Late Jurassic to Early Cretaceous [13,17,23,49–53,55,56]. According to other studies, the ages of quartz porphyry dykes associated with some CTGDs are similar to those linked to the regional mineralization of Au [49]. Plutons discovered in the Triassic Youjiang Basin [57,58] using aeromagnetic survey data support a genetic association between quartz porphyry dykes and Au mineralization in the area [49,51,52,55,59,60]. Therefore, based on systematic studies using fluid inclusions, traditional isotopes (C-H-O-S), and the composition of basement rocks, which do not outcrop in the study area [13,61–64], Au mineralization in the "Golden Triangle" is suggested to be the Carlin type in the north and orogenic type in the south [65].
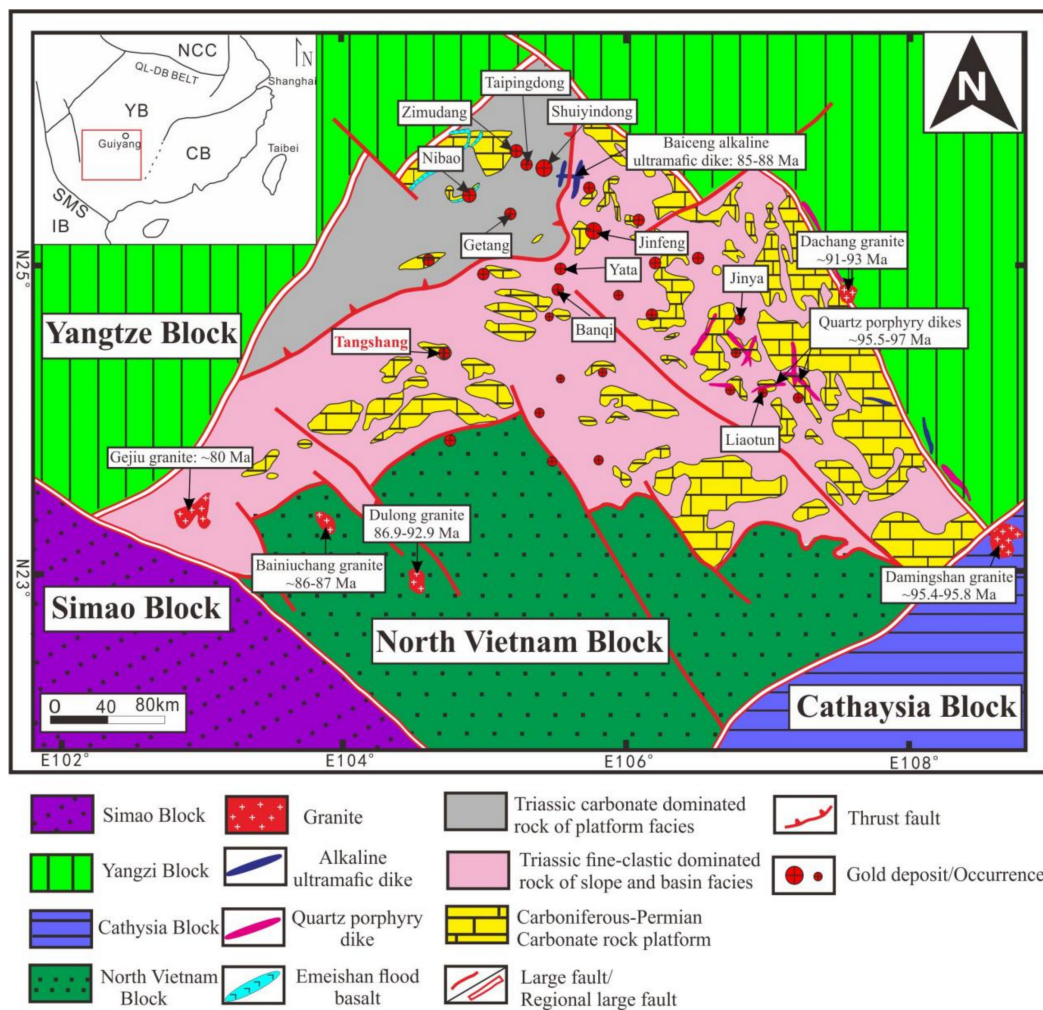
Figure 1. Map showing the regional geology of the study area and the distribution of Carlin-type Au deposits in the Yunnan–Guizhou–Guangxi "Golden Triangle" (modified from [4,17,33]). NCC: North China Craton; IB: Indo-China Block; YB: Yangtze Block; CB: Cathaysia Block; QL-DB: Qinling Dabie; and SMS: Song Ma Suture.

2.2. Deposit Geology

The Tangshang deposit is a middle-sized Au deposit located in the EW-trending Wenshan Anticline within the Wenshan autonomous prefecture in the southern Youjiang Basin. Four Au ore blocks (Saiya, Yezhuchong, Bodanshan, and Anlongshan, from southeast to northwest) are distributed in this mining area (Figure 2). However, the gold orebodies controlled by faults in Triassic strata (Saiya and Yezhuchong ore blocks) have been mined out and backfilled. Therefore, we used samples from primary gold orebodies newly found in the Emeishan Basalt Formation as the research object. The Wenshan Anticline structure and its NE- and NW-trending faults control the local Au mineralization (Figure 2). The geometry of the Au orebodies is generally controlled by main faults and their secondary structures. Bioclastic limestones and calcareous clastic rocks interbedded with argillaceous rocks from the Middle Permian to Late Triassic ages are exposed in the Wenshan Anticline (Figure 2), and several groups of N–W-, N–E-, and S–E-trending fault systems are also developed in the mining area (Figure 2). The main rocks in the area include limestones in the Middle Permian Qixia and Maokou Formations (P_2q+m), the Upper Permian Emeishan Basalt (P_3em), siltstones in the Upper Permian Nasuo and Changxing Formations (P_3n+c), calcareous mudstones in the Middle Triassic Luolou Formation, silty mudstones in the Middle Triassic Longzhang Formation, as well as sandstones and mudstones in the Upper Triassic Banna and Lanmu Formations, respectively. A peculiar feature referred to as a

structural alteration body (SBT), which is attributed to tectonic slippage and hydrothermal alteration, developed along the unconformity between the Middle Permian Maokou (P$_2$m) and Upper Permian Emeishan Basalt (P$_3$em) Formations. The SBT is the most direct marker for prospecting and an important indicator for the spatial location of orebodies. Observations at outcrops and cross-sections (Figures 2 and 3) reveal that the locations of orebodies are mainly controlled by the SBT, Emeishan basalt, and Banna Formation strata. In the Tangshang deposit, orebodies principally occur as stratiform, stratiform-like, and lenticular (Figures 2 and 3), which are commonly discontinuous, with thicknesses varying from 9.1 to 56.4 m and lengths of 50–800 m [21]. Comprehensive descriptions of the geology of the Tangshang Au deposit have been provided by Gao et al., Yang et al., and Li [20,21,39]. In general, compared with the Carlin-type gold deposits in the north of Youjiang Basin (southwest Guizhou Province) and Nevada, USA, the Tangshang gold deposit has similarities in ore controlling structure types, host rocks, and main alteration types, but the ore grade is relatively low (average grade of 1.45 g/t [39]), and there are obvious differences in geochemistry, which is also the focus of this study.
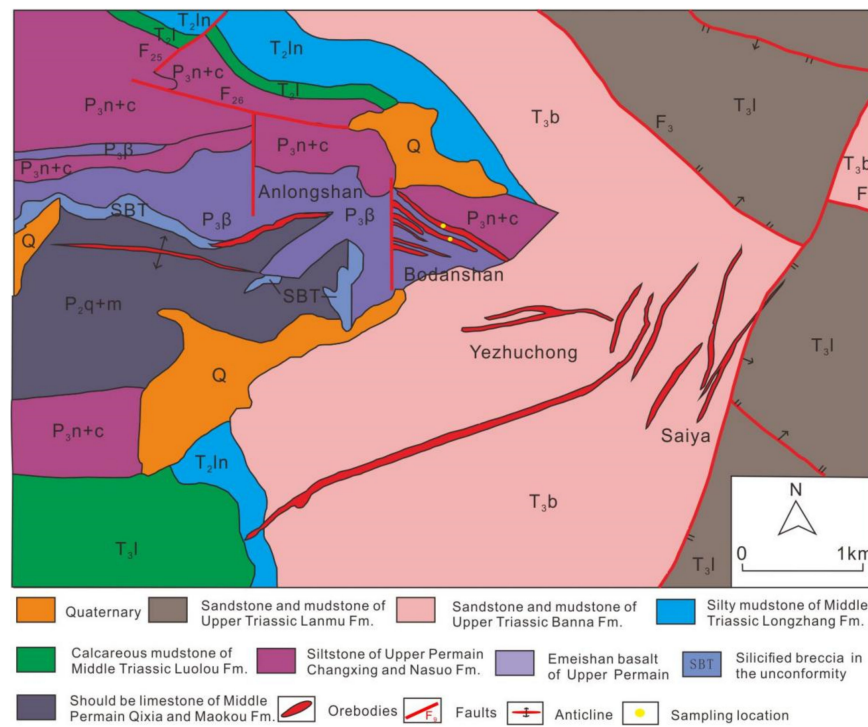
Figure 2. Map showing the geology of the Tangshang Au deposit in SE Yunnan Province (modified from [21]).
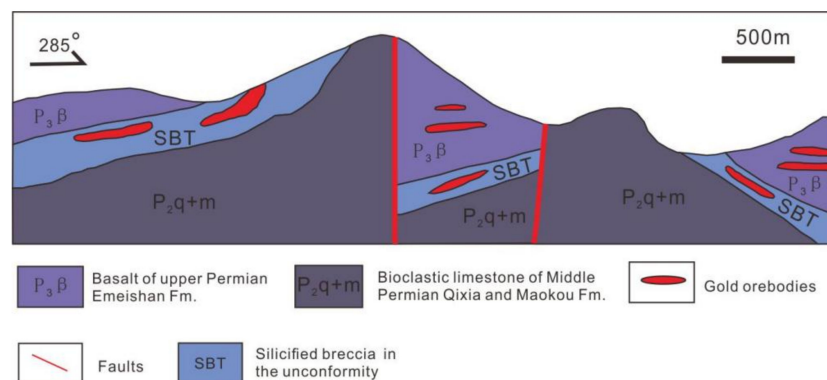
Figure 3. Cross-sectional profile of the Tangshang Au deposit (modified from [21]).

The main ore minerals in the deposit are pyrite and arsenopyrite, but limonite is abundant in oxidized ores, whereas dolomite, calcite, quartz, rutile, illite, and apatite (Figures 4 and 5) occur as gangue minerals. The ores' structures are characterized by isolated granular, disseminated, zonal, veinlet, and cataclastic formations. The types of hydrothermal alteration identified in the ores include sulfidation, silicification, kaolinization, illitization, and carbonatization. Different from the late-ore stage of typical Carlin-type gold deposits, realgar and orpiment were not recognized in the Tangshang gold deposit, which is also one of the most important differences between the Tangshang gold deposit and the typical Carlin-type gold deposit. Silicification involves sheet and vein types, and this occurs throughout the Au mineralization period. Carbonatization is reflected through the presence of calcite, dolomite veinlets, and stockworks in the ores. In contrast, argillic alteration, which involves kaolinite and illite, mainly occurs in the interstices of crystals associated with the main and late stages of ore development. According to the mineral assemblages and textural characteristics, the metallogenic stages in the Tangshang Au deposit included the following: (1) the early-ore stage of quartz–sulfides. In this stage, the Au-bearing fluids initially entered the host rock; extensive Fe-bearing mineral dissolution and silicification occurred, and at the same time, early-stage sulfides with high brightness, smooth surfaces, and high Au content were formed. (2) The main-ore stage of quartz–sulfide–rutile–apatite–clay minerals. In this stage, planar silicification occurred, along with the formation of large quantities of rutile and sulfides, with the latter being distributed in isolated and fine-grained forms. Pyrite is irregularly shaped and forms a characteristic core–rim structure. Pyrite that formed in this stage has higher brightness and Au content than that formed in the previous stage. Kaolinite and illite mainly occurred in the interstices between mineral crystals in the main-ore stages. (3) Late-stage pyrite–calcite–stibnite–clay minerals. In this stage, a small amount of granular and vein stibnite formed in the cracks of the quartz veins. The carbonate minerals precipitated to form calcite veins, with the precipitation of a small amount of fine-grained pyrite and illite. (4) The post-ore stage of limonite–hematite. In this stage, Au-bearing minerals, such as pyrite, were oxidized to form limonite, which resulted in decreased As and S contents and increased Au content. Figure 6 summarizes the mineral paragenesis relationship for each ore stage.
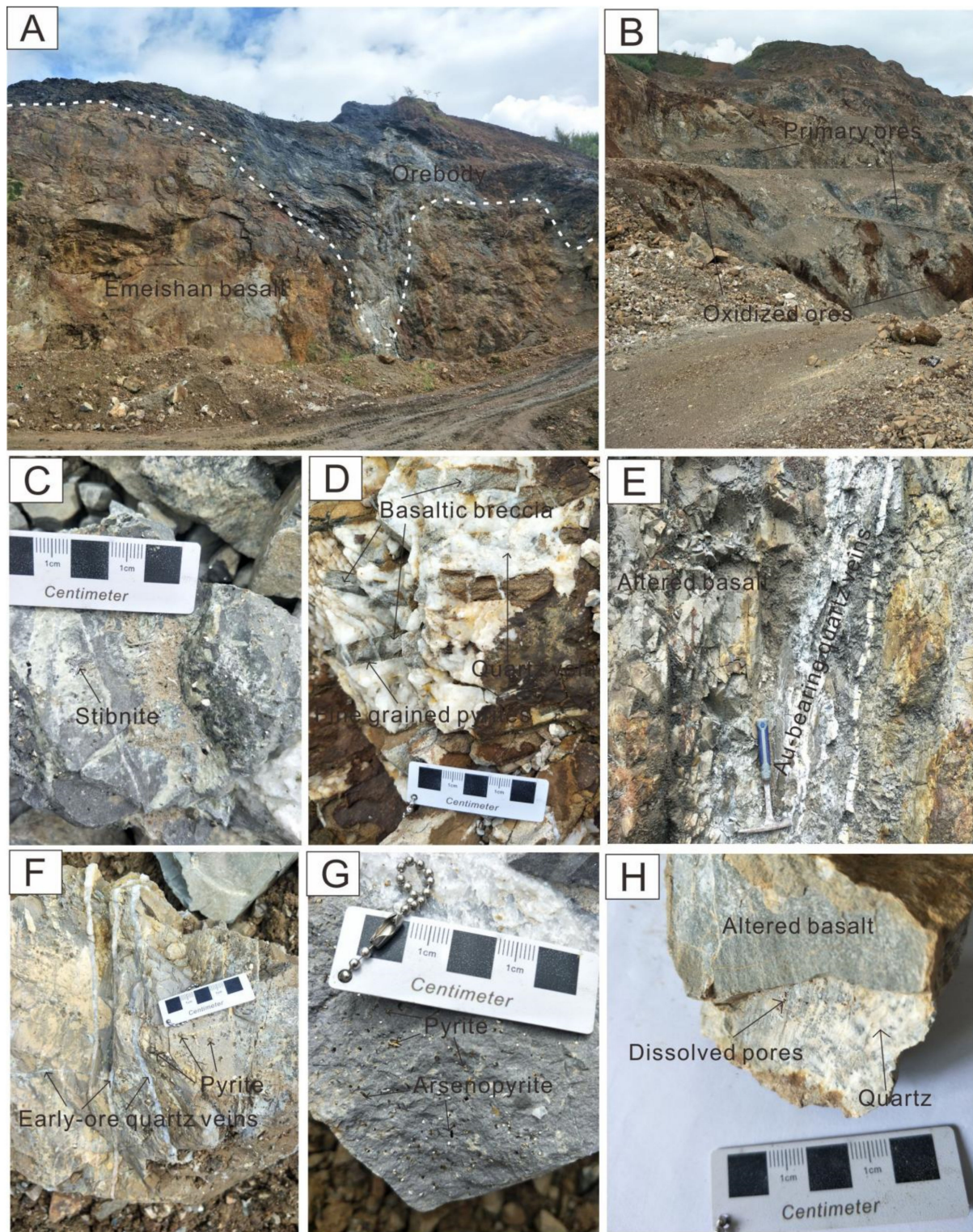
Figure 4. Illustration of typical features of Au orebodies and ores in the Tangshang Au deposit including the (**A**) surface mining landscape of the Bodanshan ore block, (**B**) primary and oxidized ores, (**C**) radially shaped stibnite in quartz veins, (**D**) basaltic breccia and quartz veins in the primary orebody exhibiting abundant fine-grain pyrite at boundaries, (**E**) altered basalt and Au-bearing quartz veins, (**F**) early-ore-stage dodecahedral pyrite and quartz veins, (**G**) dodecahedral pyrite and columnar arsenopyrite, and (**H**) dissolution pores in altered basalt.
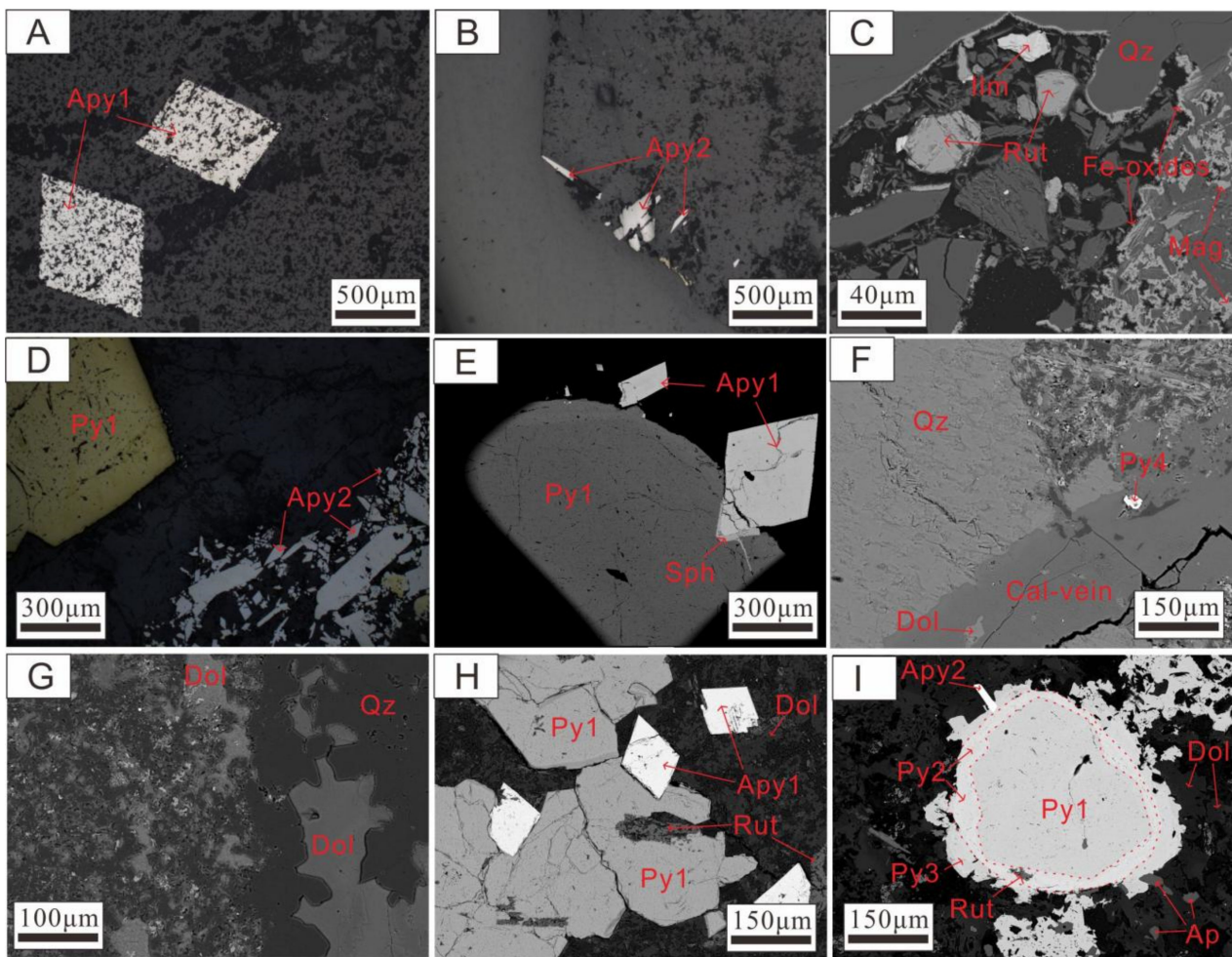
Figure 5. Morphological and textural features of different minerals in the Tangshang Au deposit including the (**A**) coarse-grained euhedral Apy1 (RPPL image), (**B**) coarse- and fine-grained Apy2 207 (RPPL image), (**C**) Ilm, Mag, and their oxides (BSE image), (**D**) early-ore dodecahedral Py1 and coarse- and fine-grained Apy2 (RPPL image), (**E**) early-ore dodecahedral Py1 and euhedral Apy1, during which fractures and contacts between pyrite and arsenopyrite were filled with sphalerite (BSE image), (**F**) a calcite vein cross-cutting a quartz vein, and Py4 and dolomite present in the calcite vein (BSE image), (**G**) dolomite veins within quartz veins (BSE image), (**H**) Py1 symbiosis with Apy1 and Rut (BSE image), and (**I**) Py2 overgrown by Py1, Py3 symbiosis with Apy2 and overgrown by Py2, Py3 symbiosis with subhedral hydrothermal Ap, and Py2 symbiosis with Rut (BSE image). Abbreviations. Apy: arsenopyrite; Py: pyrite; Qz: quartz; Rut: rutile; Ilm: ilmenite, Mag: magnetite; Ap: apatite; Dol: dolomite; and Stb: stibnite. BSE: backscattered electron; and RPPL: reflected plane polarized light.

Minerals	Ore forming stages			Post-ore stage
	Early-ore stage	Main ore stage	Late ore stage	
Py1	▬▬▬			
Py2		▬▬▬		
Py3			▬▬▬	
Py4			▬▬	
Apy1	▬▬▬			
Apy2		▬▬▬		
Stibnite			────	
Apatite		────────────		
Rutile	────────────────────			
Calcite			▬▬▬▬	
Dolomite	▬▬▬▬▬▬▬▬▬▬▬▬▬▬▬▬			
Quartz	▬▬▬▬▬▬▬▬▬▬▬▬▬▬▬▬▬▬▬▬▬			
Illite		▬▬▬		
Hematite				▬▬▬
Chlorite				▬▬▬

Figure 6. Paragenetic sequences from the early- to post-ore stages of the Tangshang Au deposit.

3. Samples and Analytical Methods

3.1. Sample Preparation

More than 40 ore samples were collected from the cross-section of an outcrop in the Bodanshan block (Figure 2), and 29 laser sections were prepared and polished to a thickness of approximately 100 μm for geochemical analyses. All sections were observed via optical microscopy and scanning electron microscopy (SEM) to identify minerals, their symbiotic relationships, and structural characteristics. Based on the generated data and comprehensive evaluation, coarse-grained sulfide minerals assigned to different ore stages were selected for use in in situ analyses using LA-ICP-MS. In situ analyses also involved Sr and S isotopes for calcite and sulfide crystals located adjacent to the position from which the associated sample used in the screening analyses was collected. (Results are presented in Tables 1–6).

Table 1. Data for major and trace elements in different types of pyrites in the Tangshang Au deposit obtained from LA-ICP-MS analyses.

Pyrite Type	Spot No.	S (wt. %)	Fe (wt. %)	As (wt. %)	Ti (ppm)	Co (ppm)	Ni (ppm)	Cu (ppm)	Total (wt. %)
Py1	TS-3-01-04	34.8	55.1	4.7	5.9	9.9	8.9	30.7	94.6
	TS-3-01-06	35.4	55.0	4.4	7.1	5.7	4.6	30.9	94.8
	TS-3-01-10	33.0	58.3	4.1	5.3	25.8	29.7	23.3	95.4
Py2	TS5-2-05-03	34.1	55.8	4.3	517	247	447	88	94.4
	TS5-2-05-06	36.2	49.4	6.5	2298	43	65	102	92.4
	TS5-2-05-08	38.5	51.3	4.5	1489	60	171	24	93.8
	TS5-2-05-09	41.8	47.0	4.9	1702	192	393	32	93.8
	TS3-2-03-03	35.1	54.6	4.2	817	986	1598	43	94.8
	TS-3-01-08	33.8	53.8	5.8	4.4	4.0	21.2	44	93.8
Py3	TS-3-01-01	31.2	54.6	6.3	17.5	1199	310	71	92.5
	TS5-2-05-04	34.1	54.8	5.0	3.0	142	252	92	94.2
	TS5-2-05-05	37.5	52.7	4.4	153	257	664	16.8	94.5
	TS5-2-05-07	39.7	50.7	4.4	6.7	19.5	61	10.8	94.8
	TS3-2-03-04	37.8	51.5	4.9	636	196	294	20.1	94.1
	TS3-2-03-07	37.6	53.6	4.0	594	158	375	11.2	95.1
	TS3-2-03-08	35.8	54.9	4.3	171	357	759	14.9	95.1
Py4	TS-3-01-07	34.6	54.5	5.0	5.3	1.7	2.3	41	94.1
	TS-3-01-05	31.8	58.5	4.5	5.6	20.6	40	89	94.8
	TS-3-01-09	33.5	57.4	4.3	4.7	5.2	4.2	14.3	95.2

Table 2. Trace element data (ppm) for different generations of pyrites from the Tangshang Au deposit obtained using LA-ICP-MS.

Pyrite Type	Spot No.	Co	Ni	Cu	Sb	Ti	Au	Tl	W	V
Py1	TS-3-01-04	9.9	8.8	30.7	9.4	5.8	5.1	bdl	bdl	bdl
	TS-3-01-06	5.7	4.6	30.8	2.7	7.0	3.9	bdl	bdl	bdl
	TS-3-01-10	25.7	29.7	23.3	bdl	5.2	4.1	bdl	bdl	bdl
Py2	TS5-2-05-03	247	447	88.3	50.9	517	12.2	1.6	2.4	7.9
	TS5-2-05-06	43.3	65.1	102	32.3	2298	38.1	bdl	6.2	25.4
	TS5-2-05-08	60.9	171	24.0	111	1489	16.6	bdl	6.5	19.1
	TS5-2-05-09	192	393	32.6	33.5	1702	13.2	bdl	9.3	17.7
	TS3-2-03-03	986	1598	43.6	130	817	6.4	0.9	0.8	9.1
	TS-3-01-08	4.0	21.1	44.9	13.6	4.4	4.8	bdl	bdl	bdl
Py3	TS-03-01-01	1,199	310	71.0	117	17.5	5.5	0.9	0.1	0.9
	TS5-2-05-04	142	252	92.1	6.3	3.0	23.6	bdl	bdl	bdl
	TS5-2-05-05	257	664	16.8	3.2	153	8.4	bdl	0.5	1.3
	TS5-2-05-07	19.5	61.7	10.8	25.3	636	5.9	bdl	bdl	bdl
	TS3-2-03-04	196	294	20.1	58.6	594	6.8	0.3	6.7	10.4
	TS3-2-03-07	158	375	11.2	63.1	171	3.6	bdl	6.4583	6.3
	TS3-2-03-08	357	759	14.9	80.6	5.3	4.4	0.1	0.8	4.9
Py4	TS-3-01-07	1.7	2.3	41.7	95.5	5.6	3.0	1.3	bdl	bdl
	TS-3-01-05	20.6	40.9	89.7	343.4	4.7	6.6	3.2	bdl	bdl
	TS-3-01-09	5.2	4.2	14.3	1.2	5.8	3.1	bdl	bdl	0.2

Abbreviations: bdl = below detection limit.

Table 3. Sulfur isotope data (‰) for different types of pyrite and arsenopyrite in the Tangshang Au deposit determined using LA-MC-ICP-MS.

Types	Stages	Spot No.	$\delta^{34}S_{V\text{-}CDT}$ (‰)
Apy1	Early-ore stage	TS-5-2-05-1	11.29
		TS-3-1-05-1	11.59
		TS-3-1-05-2	11.25
		TS-5-2-05-2	11.71
		TS-5-2-05-4	12.05
		TS-5-2-05-5	11.78
Py1	Early-ore stage	TS-3-1-05-3	11.91
		TS-3-1-05-4	11.76
		TS-3-1-05-6	12.21
		TS-3-1-05-7	12.64
		TS-3-1-02-12	12.06

Table 3. *Cont.*

Types	Stages	Spot No.	$\delta^{34}S_{V\text{-}CDT}$ (‰)
		TS-3-1-02-1	8.39
		TS-3-1-02-5	7.41
Apy2	Main-ore stage	TS-3-1-02-7	5.39
		TS-3-1-02-11	10.08
		TS-3-1-02-13	8.92
		TS-3-1-02-2	7.75
		TS-3-1-02-3	7.66
Py2	Main-ore stage	TS-3-1-02-4	8.19
		TS-3-1-02-6	7.40
		TS-3-1-02-10	9.89
		TS-5-2-05-3	11.60
Py3	Late-ore stage	TS-3-1-05-5	9.98
		TS-3-1-05-8	11.79
		TS-3-1-02-9	11.05
Py4	Late-ore stage	TS-3-1-02-8	10.59

Table 4. Trace element data (ppm) for calcite from the Tangshang Au deposit measured using LA-ICP-MS.

Spot No.	Mn	Fe	Sr	Na	P	Cr	Ba	K	Al	Rb
TS-2-01	2857	1695	452	23.7	38.7	3.5	3.9	bdl	0.4	bdl
TS-2-02	2714	1617	561	23.6	35.0	3.9	2.4	1.1	bdl	0.02
TS-2-03	1679	925	402	10.7	21.8	5.1	1.4	bdl	0.7	0.06
TS-2-04	2720	1373	506	bdl	31.4	6.1	18.9	0.1	3.2	bdl
TS-2-05	2239	1383	505	bdl	31.4	6.3	1.8	bdl	1.0	bdl
TS-2-06	1961	1263	606	47.8	26.2	4.5	3.2	1.9	0.5	bdl
TS-2-07	3836	2040	640	16.8	27.4	12.3	5.2	5.4	0.7	bdl
TS-2-08	2714	2060	740	31.7	19.2	3.4	4.7	1.6	0.2	bdl
TS-2-09	3425	2270	876	bdl	32.0	4.7	4.1	1.7	0.1	bdl
TS-2-10	1797	1343	362	bdl	31.2	4.3	1.8	0.4	3.4	bdl

Abbreviations: bdl = below detection limit.

Table 5. Rare earth element (REE) composition (ppm) of calcite from the Tangshang Au deposit measured using LA-ICP-MS.

Spot No.	La	Ce	Pr	Nd	Sm	Eu	Gd	Tb	Dy	Ho	Er	Tm	Yb	Lu	LREE	HREE	Ce/Ce*	Eu/Eu*
TS-2-01	1.8	5.1	0.7	3.9	1.0	0.8	1.0	0.1	0.8	0.1	0.3	bdl	0.3	bdl	13.3	2.6	1.06	2.18
TS-2-02	0.4	1.1	0.1	1.1	0.2	0.1	0.4	0.1	0.4	0.1	0.2	bdl	0.2	bdl	3.0	1.5	1.04	0.90
TS-2-03	0.1	0.3	0.1	0.4	0.1	0.1	0.3	0.1	0.4	0.1	0.2	bdl	0.2	bdl	1.1	1.3	0.91	0.85
TS-2-04	1.8	5.4	0.8	4.6	1.2	0.5	1.4	0.2	1.2	0.2	0.7	0.1	0.6	0.1	14.3	4.5	1.03	1.17
TS-2-05	0.5	1.4	0.2	1.3	0.4	0.1	0.6	0.1	0.6	0.1	0.3	bdl	0.4	0.1	3.9	2.2	0.99	0.77
TS-2-06	5.2	12.7	1.7	8.4	1.8	1.6	1.7	0.2	1.2	0.2	0.5	0.1	0.5	0.1	45.7	4.5	1.00	2.46
TS-2-07	1.4	4.4	0.7	3.9	1.2	0.7	1.1	0.2	1.1	0.1	0.4	0.1	0.4	0.1	12.3	3.5	1.06	1.70
TS-2-08	1.4	3.2	0.4	2.0	0.5	0.6	0.5	0.1	0.3	0.1	0.1	bdl	0.1	bdl	8.1	1.2	0.97	2.99
TS-2-09	1.0	3.2	0.5	3.1	1.0	0.5	1.0	0.1	1.0	0.2	0.4	0.1	0.4	0.1	9.5	3.3	1.02	1.53
TS-2-10	0.3	0.9	0.1	1.0	0.2	0.1	0.3	0.1	0.3	0.1	0.2	0.1	0.2	bdl	2.6	1.3	1.02	1.63
Ave.	1.4	3.8	0.5	3.0	0.8	0.5	0.8	0.1	0.7	0.1	0.3	0.1	0.3	bdl	10.0	2.4	1.01	1.62

Abbreviations: bdl = below detection limit.

Table 6. Strontium isotope ratios of calcite from the Tangshang Au deposit measured using LA-MC-ICP-MS.

Spot No.	$^{87}Rb/^{86}Sr$	2σ	$^{87}Sr/^{86}Sr$	2σ
TS-2-01	0.00002	0.00003	0.70571	0.00014
TS-2-02	0.00012	0.00004	0.70591	0.00019
TS-2-03	0.00000	0.00006	0.70587	0.00026
TS-2-04	0.00001	0.00005	0.70592	0.00025
TS-2-05	0.00003	0.00006	0.70572	0.00028

Table 6. *Cont.*

Spot No.	87Rb/86Sr	2σ	^{87}Sr/^{86}Sr	2σ
TS-2-06	0.00005	0.00007	0.70557	0.00026
TS-2-07	0.00002	0.00006	0.70563	0.00022
TS-2-08	0.00003	0.00003	0.70567	0.00012
TS-2-09	0.00000	0.00003	0.70590	0.00017
TS-2-10	0.00001	0.00004	0.70622	0.00019

3.2. LA-ICP-MS Major and Trace Element Analyses

Analyses of calcite and pyrite samples were conducted by the Beijing Createch Texting Technology Co., Ltd., Beijing, China, using a RESOlution 193 nm laser ablation (LA) instrument equipped with a COMPex Pro 102 ArF excimer laser and a Micro Las optical system. Details on the analytical instrument and procedures employed in the analysis of samples were previously reported by Zhu et al. [66]. An Analytik Jena PQMS Elite ICP-MS was utilized to determine the signal intensities of different ions. He and Ar served as the ion carrier and make-up gas, respectively; these were mixed before their input into the T-connector, and the mixture was then released into the ICP. A signal-smoothing component was installed in the LA system to produce a stable signal at a low laser repetition rate of 1 Hz [67]. The diameters of laser beams used for the in situ analysis of sulfide and calcite were 24 and 50 μm, respectively, and the laser repetition rate was 8 Hz. The compositional data for sulfides were corrected using data from the USGS MASS-1 sulfide standard [68,69]. Each LA point was associated with 20 and 45 s of background and sample–signal acquisition, respectively. An offline calculation of concentrations was conducted using the ICP-MS Data Cal program [43,70]. The uncertainties and detection limits for the analyses are presented after the element content.

3.3. In Situ Sulfur Isotope Analysis

S isotope analyses of pyrite and arsenopyrite were conducted using the Nu Plasma II MC-ICP-MS equipped with a Resolution-S155 excimer ArF LA system at Beijing Createch Texting Technology Co., Ltd., Beijing, China. The 193 nm ArF excimer laser, which was homogenized via a set of beam delivery systems, was focused on the surface of the sample at a fluence of 2.5 J/cm^2. Each acquisition incorporated 30 s of background and 40 s of a spot with a diameter of 24 μm and repetition rate of 8 Hz. He (800 mL/min) was utilized as the carrier gas to efficiently purge aerosols from the ablation cell, and this gas was mixed with Ar (~0.8 L/min) in a T-connector before its entry into the ICP torch. The integration time of the Nu Plasma II was 0.3 s. The Wenshan natural pyrite crystal (GBW07267) prepared by the Chinese Academy of Geological Sciences, Beijing, China [66], was utilized as a standard, and the reproducibility of δ^{34}S measurements was better than 0.6‰.

3.4. In Situ Strontium Isotope Analysis

The Sr isotope ratios of calcite samples were also determined using the Nu Plasma II MC-ICP-MS equipped with a Resolution-S155 excimer ArF LA system at Beijing Createch Texting Technology Co., Ltd., Beijing, China. The analytical instrument and associated procedures utilized were reported by Ramos et al. [71] and Chen et al. [72], respectively. The ^{86}Sr and ^{87}Sr analyses utilized He as the carrier gas, a laser diameter of 50–150 μm, a repetition rate of 8 Hz, and a duration of approximately 40 s. The offline calculation of the concentrations of different components was conducted using the ICP-MS Data Cal program [43,69,73]. The uncertainty and detection limits of each analysis were identical to those reported by Tong et al. [74]. Following interference corrections, the mass fractionation of Sr isotopes was corrected according to a previously reported method [74].

4. Results

4.1. Occurrence and Texture of Pyrite and Arsenopyrite

Pyrite and arsenopyrite are the main Au-bearing sulfide minerals in the Tangshang deposit, with differing textural types. Based on chemical and textural analysis, four main pyrite (Py1 to 4) and two arsenopyrite types (Apy1 and Apy2) were identified. The types and origins of sulfides in the studied samples are depicted in Figure 6, and the pyrite types, compositions, and physical characteristics are described subsequently.

4.1.1. Py1

Py1 is an early-ore-stage pyrite that is widely distributed in the walls of the host basalt (Figure 4B,D,E). It displays coarse dodecahedral and subhedral crystals, and the diameters of individual microcrystals range from 100 μm to 5 mm (Figure 4B,D,E and Figure 5A,C–E,H,I). Numerous Py1 grains are surrounded by main- and late-ore-stage pyrites (Figure 5I).

4.1.2. Py2

Py2 is an important Au-bearing sulfide in the Tangshang deposit, and it occurs as zoned and disseminated crystals (Figure 5I). Mid-zoned Py2 appears as an overgrowth enclosing Py1. According to previous studies on the types of pyrites associated with sediment-hosted CTGDs in the study area, some As-bearing pyrite grains precipitated during the early stage of Au mineralization, and thus, these are usually richer in As than in Au (Xie et al., 2018b). Similar characteristics were observed in the Tangshang Au deposit. Meanwhile, the 5–45 μm thick rim Py2 overgrowths surrounding Py1 (Figure 5I) and some Py2 was encircled by late-ore-stage Py3 (Figure 5I).

4.1.3. Py3

Late-ore-stage outer-zoned Py3 commonly coexists with euhedral–subhedral arsenopyrite (Apy2) grains in ores (Figure 5I), and the grain sizes mainly range between 5 and 60 μm, even though some grains are >80 μm (Figure 5I).

4.1.4. Py4

Py4 is uncommon (Figure 4H) in the studied samples, and it is mainly present as disseminated particles in calcite veins that cut Au ores associated with hydrothermal alteration. Py4 comprises fine grains with diameters generally <60 μm, and these irregular and elliptical grains are scattered in calcite assigned to the late ore stage (Figure 5F).

4.2. Composition of Pyrite

Data obtained from in situ LA-ICP-MS analyses are presented in Tables 1 and 2. The concentrations of principal elements in pyrite associated with mineralization and the correlations are presented in Table 1 and displayed in Figure 7.

4.2.1. Major Elements in Pyrite Determined Using LA-ICP-MS

The compositions of the major elements of 19 pyrites measured via LA-ICP-MS are presented in Table 1. The concentrations of Fe (55–58 wt.%, detection limit of 0.02–0.05 wt.%), S (33–35 wt.%, detection limit of 0.3–0.7 wt.%), Ti (3.0–2298 ppm, detection limit of 1–3 ppm), As (4.1–4.7 wt.%, detection limit of 0.002–0.003 wt.%), Co (1.7–1199 ppm, detection limit of 0.6–1.4 ppm), Ni (2.3–1598 ppm, detection limit of 2.2–5.9 ppm), and Cu (10.8–102 ppm, detection limit of 0.6–1 ppm) in Py1 were lower than those in other pyrites (Table 1 and Figure 7). However, the Fe (47–58 wt.%), S (31–41 wt.%), and As (>4.0 wt.%) concentrations in Py1, Py2, Py3, and Py4 were fairly consistent (Table 1).
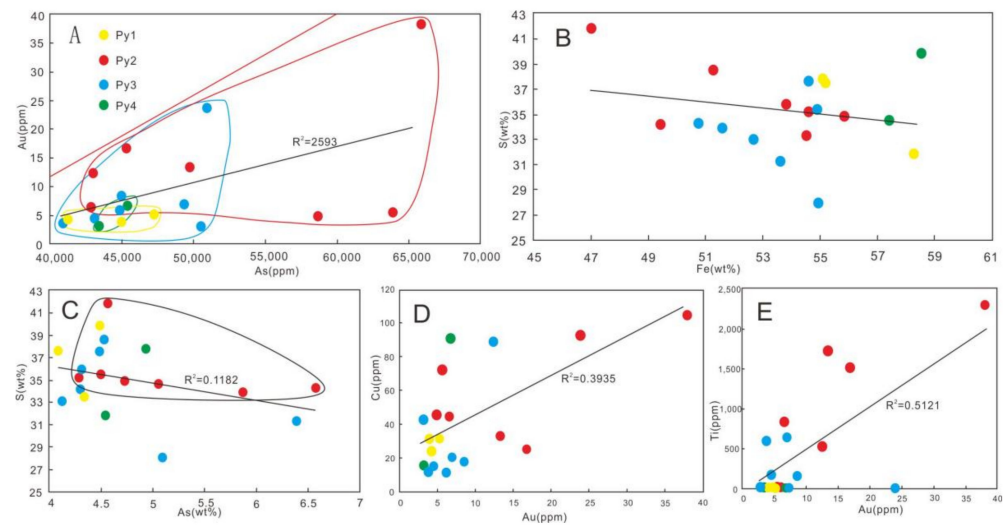
Figure 7. Elemental compositions of different types of pyrite in the Tangshang Au deposit and correlations including (**A**) As vs. Au, (**B**) S vs. Fe, (**C**) S vs. As, (**D**) Cu vs. Au, and (**E**) Ti vs. Au. The red line in Figure A means the maximum solubility of Au in pyrites. The black lines in the figures mean R^2 correlation factors. The Au saturation line in (A) was obtained from Reich et al. [75].

4.2.2. Trace Elements of Pyrite Determined Using LA-ICP-MS

The concentrations of Co, Ni, Cu, Ti, V, W, Sb, Au, and Tl in the 19 pyrites measured are presented in Table 2. Evidently, the concentrations of all trace elements analyzed increased from Py1 to Py4 (Figure 7A,B,E,F and Figure 8). The trace elements of early-ore-stage Py1 contained Au (3.9–5.1 ppm, detection limit of 0.01–0.03 ppm), Co (5.7–25.7 ppm, detection limit of 0.6–1.4 ppm), Ni (4.6–29.7 ppm, detection limit of 2.2–5.9 ppm), Cu (23.3–30.8 ppm, detection limit of 0.6–1 ppm), Ti (5.2–7.0 ppm, detection limit of 1–3 ppm), and Sb (0–9.4 ppm, detection limit of 0.1–0.2 ppm) (Table 2). Main-ore-stage Py2 had a relatively higher range of contents of Au (4.8–38.1 ppm), Cu (10.8–102 ppm), Sb (13.6–130 ppm), Tl (0–1.6 ppm, detection limit of 0.01–0.04 ppm), and W (0–9.3 ppm, detection limit of 0.02–0.07 ppm), with a large variation range in Ni (21.1–1598 ppm), Co (4.0–1199 ppm), and Ti (4.4–2298 ppm) as compared with that of Py1 (Table 2). Late-ore-stage Py3 had a relatively higher range of contents of Au (3.0–23.6 ppm), Cu (10.8–92.1 ppm), Ti (3.0–636 ppm), Co (1.7–357 ppm), Ni (2.3–759 ppm), V (0–10.4 ppm, detection limit of 1.2–3.3 ppm), Sb (3.2–95 ppm), and Tl (0–1.3 ppm) (Table 2) as compared with those of Py1. Late-ore-stage Py4 had even higher content ranges of Au (3.1–6.6 ppm), Sb (1.2–343 ppm), Cu (14.3–89.7 ppm), Ni (4.2–40.9 ppm), V (0–0.2 ppm), and Tl (0–3.2 ppm), similar to those of Py3 (Table 2). According to data presented in Figure 7A–E, Au and other elements, such as Cu, Ti, and Ni, displayed varying positive correlations (Figure 7A–E).
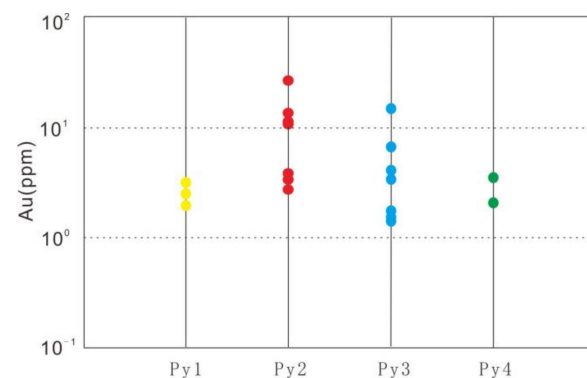
Figure 8. Plot showing the concentrations of Au (ppm) in different types of pyrite from the Tangshang Au deposit.

4.3. Sulfur Isotope Ratios of Pyrite and Arsenopyrite

The S isotope ratios of 26 representative pyrite and arsenopyrite samples were determined using LA-MC-ICP-MS, and the results are presented in Table 3 and displayed in Figure 9. Evidently, the S isotope ratios of the pyrite and arsenopyrite samples are comparable. Py1, Py2, Py3, and Py4 samples yielded δ^{34}S values varying from 11.71‰ to 12.64‰ (mean = 12.01‰), 7.40‰ to 9.89‰ (mean = 8.18‰), 9.98‰ to 11.79‰ (mean = 11.11‰), and 10.59‰ (only one sample), respectively. The values for three Apy1 samples ranged from 11.25‰ to 11.59‰ (mean = 11.38‰), whereas those for five Apy2 samples varied from 5.39‰ to 10.08 ‰ (mean = 8.04‰).
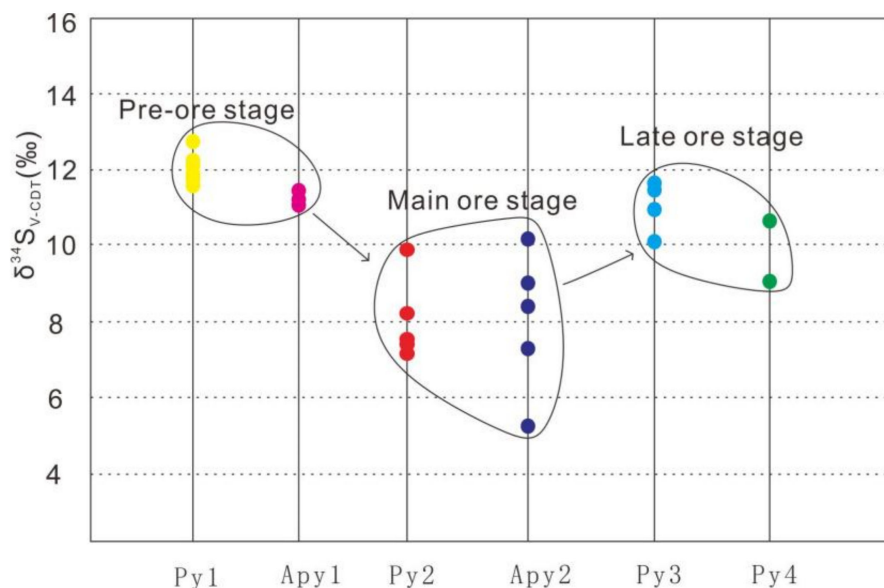
Figure 9. Plot displaying sulfur isotope ratios (‰) of different types of pyrite and arsenopyrite from the Tangshang Au deposit.

4.4. In Situ Trace and Rare Earth Element Compositions of Calcite

4.4.1. Trace Elements in Calcite

Calcite containing fine-grained Au-bearing pyrite (Py4; Figure 5F) formed during the late-ore stage. Mn, Mg, Fe, and Sr presented the highest concentrations among the analyzed elements, and the values ranged from several hundred to several thousand ppm. Na, P, Cr, and Ba represented the second most abundant elements, and their concentrations varied from a few to several dozen ppm, whereas K and Al presented the lowest concentrations with values of a few ppm (Table 4). The compositions were generally as follows: Mn (1679–3836 ppm), Fe (925–2270 ppm), Sr (362–876 ppm), Na (0–47.8 ppm), P (19.2–38.7 ppm), Cr (3.4–12.3 ppm), Ba (1.4–18.9 ppm), K (0–5.4 ppm), and Al (0–3.4 ppm) (Table 4).

4.4.2. REEs in Calcite

The total REE abundance in the calcite from the Tangshang Au deposit varied from 2.7 to 36.3 ppm (Table 5). Some samples showed light or heavy REE enrichment, whereas others exhibited flat chondrite-normalized patterns (Figure 10B). These patterns differed from those obtained from calcite assigned to the late-ore stage of sediment-hosted Shuiyindong Au deposits in southwestern Guizhou [12,76]. The REE data generated in the present study and characteristic parameters are presented in Table 5.
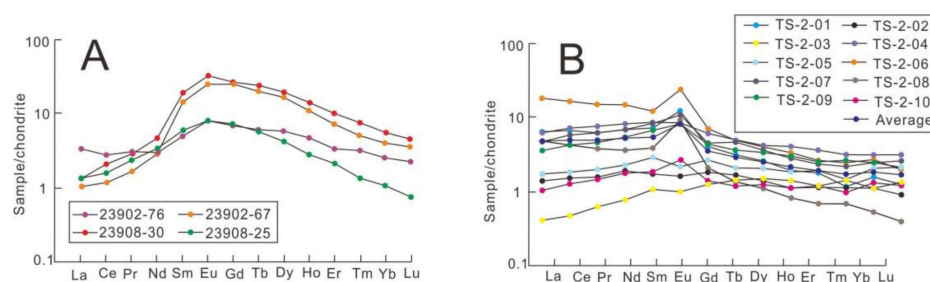
Figure 10. Chondrite-normalized plots showing REE patterns of (**A**) Au-bearing calcite veins in the Shuiyindong Au deposit [76] and (**B**) Au-bearing calcite veins in the Tangshang Au deposit (the present study).

4.5. Strontium Isotope Ratios of Calcite

The Sr isotope ratios of ten calcite samples associated with the Tangshang Au deposit are presented in Table 6. These samples produced Sr and Rb concentrations of 362–876 ppm (mean = 565 ppm) and 0–0.06 ppm, respectively. Therefore, because of the low Rb/Sr ratios of the calcite samples, the $^{87}Sr/^{86}Sr$ ratios were comparable to the original values of the hydrothermal fluids.

5. Discussion

5.1. Occurrence of Au in the Deposit

Microscopy observations revealed the absence of native Au particles in the studied samples, even in Py2, which showed the highest Au concentration of 38.1 ppm. According to the data shown in Figure 7A, the Au concentrations in the pyrites were lower than the maximum solubility of Au in pyrites [75]. Owing to the lower concentration of Au in the Tangshang Au deposit relative to others, such as the Shuiyindong, Nibao, and Zimudang deposits, determining the occurrence state of Au in the sulfides was challenging. However, the plot of Au concentrations of all pyrites below the Au saturation line (Figure 7A) suggests that hydrothermal fluids were unsaturated in Au. Therefore, Au mainly existed as nano (Au^0) and structurally bound (Au^+) particles in the interstices and lattice defect areas in the pyrites [77]. This hypothesis was confirmed by the positive correlation between Au and As reported by Hazarika et al. [31]. Similar occurrences of Au in pyrites have been reported in other CTGDs in the USA and China [26,28,29,33,77].

Based on the sulfidation and structural characteristics of pyrite in CTGDs reported in the present and previous studies, the iron vacancy created because of the replacement of S with As (Figure 7C) in the pyrite lattice is probably the main determining factor for the entry of Au and other elements (e.g., As, Cu, and Ti; Figure 7A,D,E) into pyrite. The lower concentration of Fe obtained from the Au-bearing pyrite samples relative to the theoretical concentration in pyrite supports this observation. The concentrations of Au and As in pyrite associated with hydrothermal alteration exhibit a strong positive correlation, which suggests that the precipitation of Au and As was concurrent with the crystallization of pyrite (Figure 7A).

5.2. Implications for the Origin of Au

Considering the limitation in directly analyzing Au isotopes, the S isotope characteristics of Au-bearing pyrites in Au deposits are often employed to indirectly decipher sources of Au [6,8,9,13–15,18,29]. According to previous studies based on fluid inclusions in CTGDs in the Dian–Qian–Gui district, the Au-bearing fluids were mildly acidic and characterized by intermediate to low temperatures, low salinities, low oxygen fugacity values, and high H_2S and CO_2 concentrations [6,7,11–13,16,44,45,53,78]. A prominent mechanism proposed for the precipitation of Au associated with CTGDs involves the dissolution of Fe-bearing minerals, such as pyrite, in host rocks (sedimentary or magmatic rocks), which produces Au-bearing pyrite and arsenopyrite in addition to consuming S in H_2S-rich fluids [2,11,13]. In CTGDs, pyrite and arsenopyrite are commonly the most abundant sulfide

minerals [47,79]. Moreover, because H_2S is the predominant source of S in hydrothermal systems, precipitated sulfides often exhibit similar $\delta^{34}S$ values [80,81]. Considering that no sulfate minerals were found in these ores, the $\delta^{34}S$ values of the Au-bearing sulfides likely represent the S isotope characteristics of auriferous fluids.

The LA-MC-ICP-MS analyses produced $\delta^{34}S$ ratios with ranges of 11.71–12.64‰ (mean = 12.01‰), 7.40–9.89‰ (mean = 8.18‰), 9.98–11.79‰ (mean = 11.11‰), 10.59‰ (one value), 11.25–11.59‰ (mean = 11.38‰), and 5.39–10.08‰ (mean = 8.04‰) for Py1, Py2, Py3, Py4, Apy1, and Apy2, respectively. Evidently, the S isotope ratios of the Au-bearing sulfides decreased from the early-ore stage (11.25–12.64‰) to the main-ore stage (5.37–10.08‰), which then slowly increased during the late stage (late-ore stage from 9.98–11.79‰), and then increased to values comparable to those in the early-ore stage (Table 3 and Figure 9). These results suggested that the reaction of Au-bearing fluids with Emeishan basalt dissolved Fe-bearing minerals (such as magnetite and ilmenite) in the basalt, which subsequently precipitated sulfides with slightly lower S isotope ratios during the main-ore stage. However, other sources with higher S isotope ratios are necessary to explain the higher values obtained from Au-bearing sulfides in the Tangshang deposit. Based on previous studies and data generated in the present study, the following explanations for the source of high S isotope ratios can be suggested: (1) circulating meteoric water extracted the Au from the formations and altered the Emeishan basalt to form gold deposits or (2) metamorphic fluid released from deep basement rocks dissolved Au from these rocks, and this Au-rich fluid then reacted with the Emeishan basalt to induce gold precipitation. According to previous studies, Precambrian basement rocks exposed in parts of the Dian–Qian–Gui region exhibit varying degrees of metamorphism [13,64]. Meanwhile, according to studies based on fluid inclusions and traditional isotopes, the crust in the study area can be divided into a basement and a younger caprock. Basement rocks mainly comprise Proterozoic metamorphic rocks of varying degrees, and these rocks are unexposed in the study area [13,61–64]. In addition, no Au-rich sedimentary strata were found in the study area. Therefore, metamorphic–hydrothermal fluids characterized by high S and Sr isotope ratios, which were derived from these basement rocks, are proposed as sources of the Au mineralization in the Tangshang deposit. This genetic model explains the S and Sr isotope ratios reported for the Au-bearing sulfides and calcite in the Tangshang deposit.

During the metallogenic process, Au-bearing metamorphic fluids characterized by high isotopic ratios of S and Sr were released from basement rocks, and these penetrated Emeishan basalt along structural defects. The interaction of the fluid and basalt caused the partial dissolution of Fe-bearing minerals (such as pyroxene, magnetite, and ilmenite) and enriched the hydrothermal fluid in Fe. Owing to the dissolution of Fe-bearing minerals in surrounding rocks, dilution via other fluids, and a decrease in temperature, the physicochemical conditions of the hydrothermal fluid were altered, and these changes promoted the formation of sulfides and precipitation of Au. Au-bearing pyrite (Py2) and arsenopyrite (Apy2) generated at the main-ore stage displayed the lowest S isotope ratios among all sulfide ore stages. As the water–rock interaction proceeded, most of the S in the hydrothermal fluid from Emeishan basalt was consumed because of the continuous injection of Au-bearing metamorphic fluids. Thus, the S isotope ratios of the late-ore-stage sulfides gradually became comparable to those of the early-ore-stage Py1 and Apy1.

5.3. REE Characteristics

REE data from in situ analyses of calcite samples associated with the Tangshang Au deposit display nearly flat patterns that are characterized by strong positive Eu anomalies and no prominent Ce anomalies (Figure 10B). The chondrite-normalized patterns of the calcite associated with hydrothermal alteration differed from the MREE enrichment exhibited by Au-bearing calcite in sediment-hosted CTGDs in the Dian–Qian–Gui region (Figure 10A; [76]), and the associated mechanism remains unclear. However, the strong positive Eu anomalies and the absence of a notable Ce anomaly are characteristics also displayed by Au-bearing calcites in sediment-hosted CTGDs in the Dian–Qian–Gui re-

gion [11,24,28,82]. The positive Eu anomalies are attributed to a reduction caused by hydrothermal fluids; however, the presence of abundant feldspar according to the petrographic observation of the basalt can explain this characteristic. Notably, some samples were also characterized by weak negative Eu anomalies (Figure 10). The chondrite-normalized REE patterns in fresh Emeishan basalt reported in previous studies are inclined to the right, and these highlight LREE enrichment, HREE depletion, significant positive Eu anomalies, and no Ce anomaly [56], whereas limestones from the underlying Maokou Formation show significant negative Eu anomalies [56]. The weak negative Eu anomalies can be attributed to (1) the dissolution of limestones in the underlying Maokou Formation via hydrothermal fluid and/or (2) the low REE concentrations of samples, which could enhance anomalies because of the relatively higher analytical error associated with the data (e.g., 10%). Nevertheless, the similarities and differences between the REE patterns in calcite associated with the Tangshang and sedimentary-hosted Au deposits in the Dian–Qian–Gui area [76,83,84] reveal the complexity and peculiarity of metallogenic conditions in the Tangshang Au deposit, which is an important research outcome. In addition to observations from studies on other CTGDs in the Dian–Qian–Gui region, data generated in the present study suggest that the Au-bearing fluids that formed the Tangshang Au deposit were reductive. Calcite with flat chondrite-normalized patterns and strong positive Eu anomalies has potential for tracing the occurrence of Au orebodies in Emeishan basalt.

5.4. Source of Strontium and Au-Bearing Fluids

Owing to the low Rb/Sr ratios of the calcite samples, the $^{87}Sr/^{86}Sr$ ratios were considered comparable to the initial ratios in hydrothermal fluids. Variations in the Sr isotope ratio of seawater over geological time are mainly attributed to inputs of Sr derived from the crust and mantle. Sr from the continental crust primarily originates from the weathering of rocks. Materials derived from the crust exhibit higher $^{87}Sr/^{86}Sr$ ratios (mean = 0.71190) relative to those derived from the mantle (average = 0.7035) because of the enrichment in Rb [85]. The retention time of Sr in seawater (approximately 2–4 Ma) is significantly higher than the mixing time of seawater (approximately 10^3 a), which indicates that the Sr isotope ratio of seawater is temporally and spatially uniform across the globe. Additionally, marine carbonate rocks are not associated with a notable Sr isotopic fractionation during diagenesis; their Sr isotopic ratios are similar to that of seawater [86]. The $^{87}Sr/^{86}Sr$ ratios of the Permian and Upper Devonian carbonate rocks in the study area were thus similar to those of paleo-seawater [87]. The $^{87}Sr/^{86}Sr$ ratios (0.70557–0.70622) of the calcite samples were mostly within the range of ratios reported for Emeishan basalt. Even though some values were slightly higher and fell between those of Emeishan basalt and limestone from the Maokou Formation, these values were still significantly lower than the Sr isotope ratios obtained from analyses of Upper Devonian sedimentary rocks (Figure 11). Sr isotope ratios of samples from Emeishan basalt in southwestern Guizhou Province ranged from 0.704428 to 0.705881 [88], and these were slightly lower than the values obtained from calcite samples associated with the Tangshang Au deposit. Therefore, the sources of Sr in ore-forming fluids may include (1) interactions with granites at deep positions and in the Permian/Upper Devonian strata in the shallow crust or (2) interactions between metamorphic fluids and Emeishan basalt. In addition to the in situ S isotope data for sulfides in the Tangshang Au deposit, the lithology of the basement in the area mainly comprises Proterozoic metamorphic rocks of varying degrees [61–64]. Therefore, the Tangshang Au deposit may have originated from metamorphic fluids that were diluted with meteoric water in the shallow crust.
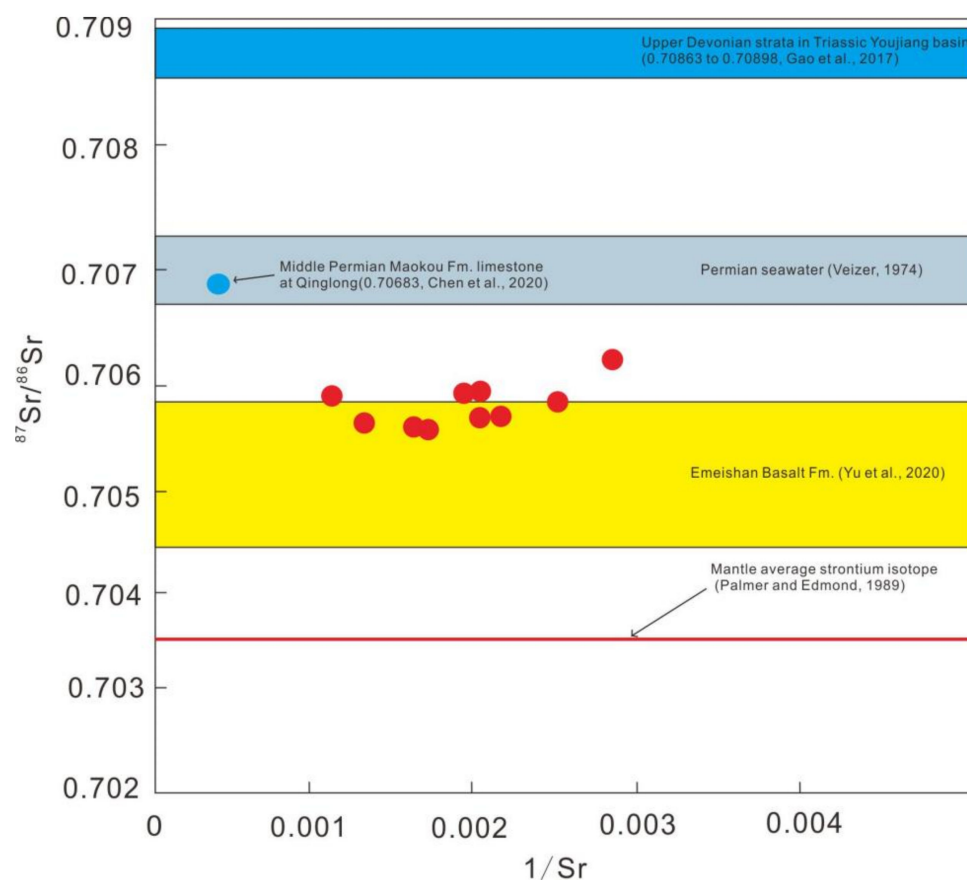
Figure 11. Plot showing the ^{87}Sr/^{86}Sr versus 1/Sr values for calcite from the Tangshang Au deposit, Upper Devonian strata in the Youjiang Basin (0.70863–0.70898, [89]), Permian seawater [87], the Emeishan Basalt Formation [88], average mantle strontium isotope composition [85], and limestone from the middle Permian Maokou Formation in Qinglong (0.70683, [25]).

5.5. Ore Deposit Genesis

The origin of the Carlin-type deposits in the Dian–Qian–Gui district has been attributed to several sources, including sedimentary, metamorphic, and magmatic sources [8,9,13,16,25–29]. The difficulty in adequately explaining the genesis of the Tangshang Au deposit is attributed to the lack of direct in situ isotope and trace elements data. The similarity of S isotope ratios for the ore-stage sulfides (Py1, Py2, Py3, Py4, Apy1, and Apy2) suggests that these originated from a common source. The results also indicate that Au-bearing hydrothermal fluids were associated with higher S isotope ratios compared with the ratios of sulfides in Emeishan basalt (0‰; [56]). Conversely, the range of ^{87}Sr/^{86}Sr ratios (0.70557–0.70622) obtained from calcite was comparable to those for Emeishan basalt. Nevertheless, some ratios were slightly higher, falling between the values from Emeishan Basalt and those for limestone from the Maokou Formation. These values were, however, significantly lower than those reported for Upper Devonian sedimentary rocks in the area (Figure 11). These results indicated that the associated fluid was enriched in S and Sr isotopes. Diverse metamorphism has been reported for the Precambrian basement rocks exposed in parts of the Dian–Qian–Gui region [61–64]. Therefore, a metamorphic source was proposed for the fluid involved in the formation of the Tangshang Au deposit. Su et al. [13] and Yang et al. [65] attributed the formation of Au deposits in the southern Dian–Qian–Gui region to metamorphic fluids, which was consistent with observations in the present study.

In summary, the Tangshang Au deposit primarily formed from Au-bearing metamorphic fluids released from basement rocks during the Indosinian orogeny or the Yanshanian orogeny of the Dian–Qian–Gui region. In addition to the Tangshang gold deposit, previous studies have shown that in many gold deposits in the southern Dian–Qian–Gui region,

metamorphic fluid participates in the metallogenic process, such as in Jinya, Nakang, and Gaolong gold deposits, and consider that the gold deposits in the southern Dian–Qian–Gui area are orogenic gold deposits of metamorphic fluid origin [13,65]. The precipitation of Au was linked to physicochemical interactions between Au-bearing fluids, meteoric water, and wall rocks. However, the contribution of Au and other elements from the sedimentary strata, especially Au-bearing black argillaceous rocks and Emeishan basalts (Au = 10–79 ppb; [56]), cannot be excluded.

6. Conclusions

In the present study, four types of pyrite (Py1, Py2, Py3, and Py4) and two types of arsenopyrite (Apy1 and Apy2) were identified in samples from the Tangshang Au deposit. REE data from the in situ analyses of calcite exhibited flat patterns with prominent positive Eu anomalies but without notable Ce anomalies. These results suggest that the Au-bearing fluid that produced the deposit was reducing in character. The ore-forming fluid had a higher $\delta^{34}S$ and $^{87}Sr/^{86}Sr$ compared with those in the host Emeishan basalt. Based on the predominant presence of basement Proterozoic metamorphic rocks in varying degrees in the Dian–Qian–Gui region and data generated in the present study, derivation from deep-seated metamorphic basement rocks was proposed for the Au in the Tangshang deposit and the associated Au-bearing fluids and indicated a gold mineralization event related to metamorphic fluid in the south of the Dian–Qian–Gui "Golden Triangle".

Author Contributions: Conceptualization, Investigation and Methodology, Data curation, Writing—original draft, Writing—review and editing, W.S.; Funding acquisition, W.S., J.L. (Jianzhong Liu), and L.Z.; Investigation and Methodology, P.W., J.L. (Junhai Li), Z.W., Z.X. and Q.T.; Project administration, W.S., L.Z. and J.L. (Jianzhong Liu); Experimental data consolidation, W.S.; Writing—original draft, W.S.; and Writing—review and editing, W.S., P.W. and Z.X. All authors have read and agreed to the published version of the manuscript.

Funding: This study was jointly funded by the Talent Team Program of Science and Technology Foundation of Guizhou Province (Qian Ke He Ping Tai Ren Cai CXTD[2021]007), the National Natural Science Fund of China (U1812402), the National Key Research and Development Program of China, "Exploration and Exploitation of Deep Earth Resources" (2017YFC0601500), the National Natural Science Fund of China (41962008), and the Guizhou Province Graduate Research Fund (YJSCXJH [2020]095).

Data Availability Statement: Not applicable.

Acknowledgments: We thank the NO. 105 Geological Party of the Guizhou Bureau of Geology and Mineral Exploration & Development for conducting the field work. We are also grateful to Shaohua Dong for assistance during the BSE, SEM, and EDS analyses and E. Dewei Kong for the support provided when conducting the trace element and isotopic analyses of the sulfides and calcite. We would like to thank the anonymous reviewers for their constructive comments.

Conflicts of Interest: The authors declare no conflict of interest.

References

1. Dobra, J.L. The US gold industry 1996. *Nev. Bur. Mines Geol. Spec. Publ.* **1997**, *31*, 1545.
2. Cline, J.S.; Hofstra, A.H.; Muntean, J.L.; Tosdal, R.M.; Hickey, K.A. Carlin-type gold deposits in Nevada: Critical geologic characteristics and viable models. *Econ. Geol.* **2005**, *10*, 451–484.
3. Hu, X.L.; Gong, Y.J.; Zeng, G.P.; Zhang, Z.J.; Wang, J.; Yao, S.Z. Multistage pyrite in the Getang sediment-hosted disseminated gold deposit, southwestern Guizhou Province, China: Insights from textures and in situ chemical and sulfur isotopic analyses. *Ore Geol. Rev.* **2018**, *99*, 1–16. [CrossRef]
4. Yan, J.; John, A.M.; Liu, S.; Ian, M.C. Fluid properties and origins of the Lannigou Carlin-type gold deposit, SW China: Evidence from SHRIMP oxygen isotopes and LA-ICP-MS trace element compositions of hydrothermal quartz. *J. Geochem. Explor.* **2020**, *215*, 1–14. [CrossRef]
5. Arehart, G.B. Characteristics and origin of sediment-hosted disseminated gold deposits: A review. *Ore Geol. Rev.* **1996**, *11*, 383–403. [CrossRef]
6. Hofstra, A.H.; Cline, J.S. Characteristics and models for Carlin-type gold deposits. *Rev. Econ. Geol.* **2000**, *11*, 163–220.

7.   Hu, R.Z.; Su, W.C.; Bi, X.W.; Tu, G.Z.; Hofstra, A.H. Geology and geochemistry of Carlin-type gold deposits in China. *Mine Depos.* **2002**, *37*, 378–392.

8.   Hu, R.Z.; Chen, W.T.; Xu, D.R.; Zhou, M.F. Reviews and new metallogenic models of mineral deposits in South China: An introduction. *J. Asian Earth Sci.* **2017**, *137*, 1–8. [CrossRef]

9.   Hu, R.Z.; Fu, S.L.; Huang, Y.; Zhou, M.F.; Fu, S.H.; Zhao, C.H.; Wang, Y.J.; Bi, X.W.; Xiao, J.F. The giant South China Mesozoic low-temperature metallogenic domain: Reviews and a new geodynamic model. *J. Asian Earth Sci.* **2017**, *137*, 9–34. [CrossRef]

10. Zaw, K.; Peters, S.G.; Cromie, P.; Burrett, C.; Hou, Z.Q. Nature, diversity of deposit types and metallogenic relations of South China. *Ore Geol. Rev.* **2007**, *31*, 3–47. [CrossRef]

11. Su, W.C.; Heinrich, C.A.; Pettke, T.; Zhang, X.C.; Hu, R.Z.; Xia, B. Sediment-hosted gold deposits in Guizhou, China: Products of wall-rock sulfidation by deep crustal fluids. *Econ. Geol.* **2009**, *104*, 73–93. [CrossRef]

12. Su, W.C.; Hu, R.Z.; Xia, B.; Xia, Y.; Liu, Y.P. Calcite Sm-Nd isochron age of the Shuiyindong Carlin-type gold deposit, Guizhou, China. *Chem. Geol.* **2009**, *258*, 269–274. [CrossRef]

13. Su, W.C.; Dong, W.D.; Zhang, X.C.; Shen, N.P.; Hu, R.Z.; Hofstra, A.H.; Cheng, L.Z.; Xia, Y.; Yang, K.Y. Carlin-type gold deposits in the Dian-Qian-Gui "Golden Triangle" of southwest China. *Rev. Econ. Geol.* **2018**, *20*, 157–185.

14. Large, R.R.; Bull, S.W.; Maslennikov, V.V. A carbonaceous sedimentary source-rock model for Carlin-type and orogenic gold deposits. *Econ. Geol.* **2011**, *106*, 331–358. [CrossRef]

15. Large, S.J.E.; Bakker, E.Y.N.; Weis, P.; Waelle, M.; Ressel, M.; Heinrich, C.A. Trace elements in fluid inclusions of sediment-hosted gold deposits indicate a magmatichydrothermal origin of the Carlin ore trend. *Geology* **2016**, *44*, 1015–1018. [CrossRef]

16. Peng, Y.W.; Gu, X.X.; Zhang, Y.M.; Liu, L.; Wu, C.Y.; Chen, S.Y. Ore-forming process of the Huijiabao gold district, southwestern Guizhou Province, China: Evidence from fluid inclusions and stable isotopes. *J. Asian Earth Sci.* **2014**, *93*, 89–101. [CrossRef]

17. Chen, M.H.; Mao, J.W.; Li, C.; Zhang, Z.Q.; Dang, Y. Re-Osisochron ages for arsenopyrite from Carlin-like gold deposits in the Yunnan-Guizhou-Guangxi "golden triangle", southwestern China. *Ore Geol. Rev.* **2015**, *64*, 316–327. [CrossRef]

18. Groves, D.I.; Goldfarb, R.J.; Santosh, M. The conjunction of factors that lead to formation of giant gold provinces and deposits in non-arc settings. *Geosci. Front.* **2016**, *7*, 303–314. [CrossRef]

19. Tu, G.C. The uranium and gold metallogenic belts in SW Qinling and the SW Guizhou, and their similarities to the Carlin-type gold deposits in the western America. *Uranium Geol.* **1990**, *6*, 322–325. (In Chinese)

20. Li, Y.C. A summary of the genesis of gold deposit in guangnan county, yunnan province. *World Nonf. Met.* **2017**, *3*, 147–149.

21. Yang, C.H.; She, Z.M.; Cheng, S.F. Discussion on genesis of Tangshang gold deposit in Yunnan. *Miner. Explor.* **2013**, *4*, 387–394.

22. Zhang, J.; Su, Q.W.; Liu, X.F.; He, Z.H.; Zhou, Y.M.; Li, Z.; Zhao, K. Characteristics of geology and isotopic geochemistry of the Laozhaiwan gold deposit in southeastern Yunnan Province, China. *Acta Petrol.* **2014**, *9*, 2657–2668.

23. Pi, Q.H.; Hu, R.Z.; Xiong, B.; Li, Q.L.; Zhong, R.C. In situ SIMS U-Pb dating of hydrothermal rutile: Reliable age for the Zhesang Carlin-type gold deposit in the golden triangle region, SW China. *Miner Deposit.* **2017**, *52*, 1179–1190. [CrossRef]

24. Zhang, Y.; Xia, Y.; Su, W.C. Metallogenic model and prognosis of the Shuiyindong super-large strata-bound Carlin-type gold deposit, southwestern Guizhou Province, China. *Chin. J. Geochem.* **2010**, *29*, 157–166. [CrossRef]

25. Chen, J.; Yang, R.D.; Du, L.J.; Gao, J.B.; Zheng, L.L.; Huang, Z.L. Multistage fluid sources and evolution of Qinglong Sb-(Au) deposit in northern margin of Youjiang basin, SW China: REE geochemistry and Sr-H-O isotopes of ore-related jasperoid, quartz and fluorite. *Ore Geol. Rev.* **2020**, *127*, 1–18. [CrossRef]

26. Su, W.C.; Xia, B.; Zhang, H.T.; Zhang, X.C.; Hu, R.Z. Visible gold in arsenian pyrite at the Shuiyindong Carlin-type gold deposit, Guizhou, China: Implications for the environment and processes of ore formation. *Ore Geol. Rev.* **2008**, *33*, 667–679. [CrossRef]

27. Liu, J.Z.; Chen, J.H.; Deng, Y.M.; Fu, Z.K.; Chen, F.E.; You, B. Exploration of the Shuiyingdong super-scale gold deposit and the evolution of exploration for metallogenic belt of the Huijiabao anticline in Guozhou Province. *Geol. Surv. Res.* **2009**, *32*, 138–143. (In Chinese with English abstract)

28. Wang, Z.P. Genesis and Dynamic Mechanism of the Epithermal Ore Deposits, SW Guizhou, China. A Case Study of Gold and Antimony Deposits. Ph.D. Thesis, Institute of Geochemistry, Chinese Academy of Sciences, Guiyang, China, 2013; pp. 1–150. (In Chinese with English abstract)

29. Xie, Z.J.; Xia, Y.; Cline, J.S.; Pribil, M.J.; Koenig, A.; Tan, Q.P.; Wei, D.T.; Wang, Z.P.; Yan, J. Magmatic origin for sediment-hosted Au deposits, Guizhou Province, China: In situ chemistry and sulfur isotope composition of pyrites, Shuiyindong and Jinfeng deposits. *Econ. Geol.* **2018**, *113*, 1627–1652. [CrossRef]

30. Large, R.R.; Maslennikon, V.V.; Robert, F.; Danyushevsky, L.V.; Chang, Z.S. Multistage sedimentary and metamorphic origin of pyrite and gold in the giant Sukhoi Log deposit, Lena gold province Russia. *Econ. Geol.* **2007**, *102*, 1233–1267. [CrossRef]

31. Hazarika, P.; Mishra, B.; Chinnasamy, S.S.; Bernhardt, H.J. Multi-stage growth and invisible gold distribution in pyrite from the Kundarkocha sediment-hosted gold deposit, eastern India. *Ore Geol. Rev.* **2013**, *55*, 134–145. [CrossRef]

32. Gregory, D.D.; Large, R.R.; Bath, A.B.; Steadman, J.A.; Wu, S.; Danyushevsky, L.; Bull, S.W.; Holden, P.; Ireland, T.R. Trace element content of pyrite from the Kapai Slate, St. Ives gold district, western Australia. *Econ. Geol.* **2016**, *111*, 1297–1320. [CrossRef]

33. Xie, Z.J.; Xia, Y.; Cline, J.S.; Koenig, A.; Wei, D.T.; Tan, Q.P.; Wang, Z.P. Are there Carlin-type Au deposits in China? A comparison of the Guizhou, China, deposits with Nevada, USA. *Rev. Econ. Geol.* **2018**, *20*, 187–233.

34. Kesler, S.E.; Riciputi, L.C.; Ye, Z.J. Evidence for a magmatic origin for Carlin-type gold deposits: Isotopic composition of sulfur in the Betze-Post-Screamer deposit, Nevada USA. *Miner. Depos.* **2005**, *40*, 127–136. [CrossRef]

35. Bendall, C.; Lahaye, Y.; Fiebig, J.; Weyer, S.; Brey, G.P. In situ sulfur isotope analysis by laser ablation MC-ICPMS. *Appl. Geochem.* **2006**, *21*, 782–787. [CrossRef]

36. Chang, Z.S.; Large, R.R.; Maslennikov, V. Sulfur isotopes in sediment-hosted orogenic gold deposits: Evidence for an early timing and a seawater sulfur source. *Geology* **2008**, *36*, 971–974. [CrossRef]

37. Barker, S.L.L.; Hickey, K.A.; Cline, J.J.; Dipple, G.M.; Kilburn, M.R.; Vaughan, J.R.; Longo, A.A. Uncloaking invisible gold: Use of nanoSIMS to evaluate gold, trace elements, and sulfur isotopes in pyrite from Carlin-type gold deposits. *Econ. Geol.* **2009**, *104*, 897–904. [CrossRef]

38. Hou, L.; Peng, H.J.; Ding, J.; Zhang, J.R.; Zhu, S.B.; Wu, S.Y.; Wu, Y.; Hegen, O. Textures and in situ chemical and isotopic analyses of pyrite, Huijiabao Trend, Youjiang Basin, China: Implications for paragenesis and source of sulfur. *Econ. Geol.* **2016**, *111*, 331–353. [CrossRef]

39. Gao, Z.P.; Ren, Y.H.; Zhang, Z. Geological characteristics and prospective prognosis of the Tangshang Au deposit in Guangnan County, Yunnan Province. *Acta Geosci. Sin.* **2013**, *34*, 76–80.

40. Zhou, X.M.; Sun, T.; Shen, W.Z.; Shu, L.S.; Niu, Y.L. Petrogenesis of mesozoic granitoids and volcanic rocks in South China: A response to tectonic evolution. *Episodes* **2006**, *29*, 26–33. [CrossRef]

41. Wang, Y.J.; Fan, W.M.; Sun, M.; Liang, X.Q.; Zhang, Y.H.; Peng, T.P. Geochronological, geochemical and geothermal constraints on petrogenesis of the Indosinian peraluminous granites in the South China Block: A case study in the Hunan Province. *Lithos* **2007**, *96*, 475–502. [CrossRef]

42. Hu, R.Z.; Zhou, M.F. Multiple Mesozoic mineralization events in South China—An introduction to the thematic issue. *Miner. Depos.* **2012**, *47*, 579–588. [CrossRef]

43. Hu, X.L.; Yao, S.Z.; Ding, Z.J.; He, M.C. Early Paleozoic magmatism and metallogeny in Northeast China: A record from the Tongshan porphyry Cu deposit. *Miner. Depos.* **2017**, *52*, 85–103. [CrossRef]

44. Zhang, X.C.; Spiro, B.; Halls, C.; Stanley, C.J.; Yang, K.Y. Sediment-hosted disseminated gold deposits in Southwest Guizhou, PRC: Their geological setting and origin in relation to mineralogical, fluid inclusion, and stable-isotope characteristics. *Int. Geol. Rev.* **2003**, *45*, 407–470. [CrossRef]

45. Wang, Y.G.; Suo, S.T.; Zhang, M.F. *Tectonics and Carlin-Type Gold Deposits in Southwestern Guizhou, China*; Geology Publishing House: Beijing, China, 1994; pp. 512–516 (In Chinese with English abstract)

46. Zheng, L.L.; Yang, R.D.; Gao, J.B.; Chen, J.; Li, D.P. Quartz Rb-Sr isochron ages of two type Orebodies from the Nibao Carlin-type gold deposit, Guizhou, China. *Minerals* **2019**, *9*, 399. [CrossRef]

47. Chen, M.H.; Zhang, Z.Q.; Santosh, M.; Dang, Y.; Zhang, W. The Carlin-type gold deposits of the "golden triangle" of SW China: Pb and S isotopic constraints for the ore genesis. *J. Asian Earth Sci.* **2015**, *103*, 115–128. [CrossRef]

48. Zhang, X.J.; Xiao, J.F. Zircon U-Pb geochronology, Hf isotope and geochemistry study of the Late Permian diabases in the northwest Guangxi autonomous region. *Bull. Mineral Petrol Geochem.* **2014**, *33*, 163–176. (In Chinese with English abstract)

49. Zhu, J.J.; Zhong, H.; Xie, G.Q.; Zhao, C.H.; Xu, L.L.; Lu, G. Origin and geological implication of the inherited zircon from felsic dikes, Youjiang Basin, China. *Acta Petrol. Sin.* **2016**, *32*, 3269–3280. (In Chinese with English abstract)

50. Liu, S.; Su, W.C.; Hu, R.Z.; Feng, C.X.; Gao, S.; Coulson, I.M.; Wang, T.; Feng, G.Y.; Tao, Y.; Xia, Y. Geochronological and geochemical constraints on the petrogenesis of alkaline ultramafic dykes from southwest Guizhou Province, SW China. *Lithos* **2010**, *114*, 253–264. [CrossRef]

51. Guo, J.H. Relationship between ultramicro-grained gold mineralization and magmatism in northwest Guangxi Province, China. *J. Precious Metal. Geol.* **2000**, *9*, 133–143. (In Chinese with English abstract)

52. Huang, Y.Q.; Cui, Y.Q. The relationship between magmatic rocks and gold mineralization of Mingshan Gold deposit of Lingyun. Guangxi. *Guangxi Geol.* **2001**, *4*, 22–28. (In Chinese with English abstract)

53. Su, W.C. The Hydrothermal Fluid Geochemistry of the Carlin-Type Gold Deposits in Southeastern Yangtze Craton, China. Ph.D. Thesis, Institute of Geochemistry, Chinese Academy of Science, Guiyang, China, 2002; pp. 1–116. (In Chinese with English abstract)

54. Peters, S.G.; Huang, J.Z.; Li, Z.P.; Jing, C.G. Sedimentary rock-hosted Au deposits of the Dian-Qian-Gui area. *Ore Geol. Rev.* **2007**, *31*, 170–204. [CrossRef]

55. Li, Y.Q.; Pang, B.C.; Yang, F.; Zhang, D.W.; Zeng, Q.F.; Liu, X. Geochemical characteristics and metallogenic significance of quartz porphyry in Liaotun gold deposit, Bama County, Guangxi. *Geoscience* **2014**, *6*, 1138–1150. (In Chinese with English abstract)

56. Li, J.H. The Study of Ore-Forming Processes of the Jiadi and Damaidi Basalt-Hosted Gold Deposits, Southwestern Guizhou Province, China. Ph.D. Thesis, Guizhou University, Guiyang, China, 2021; pp. 1–169. (In Chinese with English abstract)

57. Wang, L.; Zhang, Y.W.; Liu, S.G. The application of regional gravity and magnetic data to delineating intrusive bodies and local geological structures in Guizhou Province. *Geophy. Geochem. Explor.* **2009**, *33*, 246–249. (In Chinese with English abstract)

58. Wang, L.; Long, C.L.; Liu, Y. Discussion on concealed rock mass delineation and gold source in southwestern Guizhou. *Geoscience* **2015**, *29*, 703–712. (In Chinese with English abstract)

59. Chen, M.H.; Mao, J.W.; Bierlein, F.P.; Norman, T.; Uttley, P.J. Structural features and metallogenesis of the Carlin-type Jinfeng (Lannigou) gold deposit, Guizhou Province, China. *Ore Geol. Rev.* **2011**, *43*, 217–234.

60. Ma, J.; Pang, B.; Li, P.; Yang, B.; Zhao, J. Geochemical characteristics of the quartz porphyry and its geological implications, northwest Guangxi, China. *Acta Mineral. Sin.* **2013**, *33*, 165. (In Chinese)

61. *Regional Geology of Guangxi Zhuang Autonomous Region*; Geological Publishing House, Bureau of Geology and Mineral Resources of Guangxi Zhuang Autonomous Region: Guanxi, China, 1985.

62. *Regional Geology of Guizhou Province*; Geological Publishing House, Bureau of Geology and Mineral Resources of Guizhou Province: Guizhou, China, 1987.

63. *Regional Geology of Yunnan Province*; Geological Publishing House, Bureau of Geology and Mineral Resources of Yunnan Province: Yunnan, China, 1990.

64. Du, Y.S.; Huang, H.; Yang, J.H.; Huang, H.W.; Tao, P.; Huang, Z.Q.; Hu, L.S.; Xie, C.X. The basin translation from Late Paleozoic to Triassic of the Youjiang basin and its tectonic signification. *Geol. Rev.* **2013**, *59*, 1–11. (In Chinese with English abstract)

65. Yang, L.; Deng, L.; David, I.G.; Wang, Q.F.; Zhang, L.; Wu, W.; Qin, K.; Zhang, Q.Z. Recognition of two contrasting structural-and mineralogical-gold mineralsystems in the Youjiang basin, China-Vietnam: Orogenic gold in the south and Carlin-type in the north. *Geosci. Front.* **2020**, *11*, 1477–1494. [CrossRef]

66. Zhu, Z.Y.; Jiang, S.Y.; Ciobanu, C.L.; Yang, T.; Cook, N.J. Sulfur isotope fractionation in pyrite during laser ablation: Implications for laser ablation multiple collector inductively coupled plasma mass spectrometry mapping. *Chem. Geol.* **2017**, *450*, 223–234. [CrossRef]

67. Hu, Z.C.; Zhang, W.; Liu, Y.S.; Gao, S.; Li, M.; Zong, K.Q.; Chen, H.H.; Hu, S.H. "Wave" signal-smoothing and mercury-removing device for laser ablation quadrupole and multiple collector ICPMS analysis: Application to lead isotope analysis. *Anal. Chem.* **2015**, *87*, 1152–1157. [CrossRef] [PubMed]

68. Wilson, S.A.; Ridley, W.I.; Koenig, A.E. Development of sulfide calibration standards for the laser ablation inductively-coupled plasma mass spectrometry technique. *J. Anal. At. Spectrom.* **2002**, *17*, 406–409. [CrossRef]

69. Liu, Y.S.; Hu, Z.C.; Gao, S.; Guenther, D.; Xu, J.; Gao, C.G.; Chen, H.H. In situ analysis of major and trace elements of anhydrous minerals by LA-ICP-MS without applying an internal standard. *Chem. Geol.* **2008**, *257*, 34–43. [CrossRef]

70. Hu, X.L.; Ding, Z.J.; Yao, S.Z.; He, M.C.; Shen, J.; Zhu, B.P.; Chen, B. Geochronology and Sr-Nd-Hf isotopes of the Mesozoic granitoids from the Great Xing'an and Lesser Xing'an ranges: Implications for petrogenesis and tectonic evolution in NE China. *Geol. J.* **2016**, *51*, 1–20. [CrossRef]

71. Ramos, F.C.; Wolff, J.A.; Tollstrup, D.L. Measuring ^{87}Sr/^{86}Sr variations in minerals and groundmass from basalts using LA-MC-ICP-MS. *Chem. Geol.* **2004**, *211*, 135–158. [CrossRef]

72. Chen, W.; Lu, J.; Jiang, S.Y.; Ying, Y.C.; Liu, Y.S. Radiogenic Pb reservoir contributes to the rare earth element(REE) enrichment in South Qinling carbonatites. *Chem. Geol.* **2018**, *494*, 80–95. [CrossRef]

73. Liu, Y.S.; Gao, S.; Hu, Z.C.; Gao, C.G.; Zong, K.Q.; Wang, D.B. Continental and oceanic crust recycling-induced melt-peridotite interactions in the Trans-North China Orogen: U-Pb dating, Hf isotopes and trace elements in zircons of mantle xenoliths. *J. Petrol* **2010**, *51*, 537–571. [CrossRef]

74. Tong, X.R.; Liu, Y.S.; Hu, Z.C.; Chen, H.H.; Zhou, L.; Hu, Q.H.; Xu, R.; Deng, L.X.; Chen, C.F.; Yang, L. Accurate determination of Sr isotopic compositions in clinopyroxene and silicate glasses by LA–MC–ICP–MS. *Geostand. Geoanal. Res.* **2016**, *40*, 85–99. [CrossRef]

75. Reich, M.; Kesler, S.E.; Utsunomiya, S.; Palenik, C.S.; Chryssoulis, S.L.; Ewing, R.C. Solubility of gold in arsenian pyrite. *Geochim. Cosmochim.* **2005**, *69*, 2781–2796. [CrossRef]

76. Tan, Q.P.; Xia, Y.; Wang, X.Q.; Xie, Z.J.; Wei, D.T. Carbon-oxygen isotopes and rare earth elements as an exploration vector for Carlin-type gold deposits: A case study of the Shuiyindong gold deposit, Guizhou Province, SW China. *J. Asian Earth Sci.* **2017**, *148*, 1–12. [CrossRef]

77. Simon, G.; Kesler, S.E.; Chryssoulis, S. Geochemistry and textures of gold-bearing arsenian pyrite, Twin Creeks, Nevada: Implications for deposition of gold in Carlintype deposits. *Econ. Geol.* **1999**, *94*, 405–421. [CrossRef]

78. Xie, X.Y.; Feng, D.S.; Chen, M.H.; Guo, S.X.; Kuang, S.D.; Chen, H.S. Fluid inclusion and stable isotope geochemistry study of the Nibao gold deposit, Guizhou and insights into ore genesis. *Acta Petrol. Sin.* **2016**, *32*, 3360–3376. (In Chinese with English abstract)

79. Emsbo, P.; Hofstra, A.H.; Lauha, E.A.; Griffin, G.L.; Hutchinson, R.W. Origin of high-grade gold ore, source of ore fluid components, and genesis of the Meikle and neighboring Carlin-type deposits, northern Carlin trend. *Nevada. Econ. Geol.* **2003**, *98*, 1069–1105. [CrossRef]

80. Ohmoto, H. Systematics of sulfur and carbon isotopes in hydrothermal ore deposits. *Econ. Geol.* **1972**, *67*, 551–578. [CrossRef]

81. Ohmoto, H.; Rye, R.O. Isotopes of sulfur and carbon. In *Geochemistry of Hydrothermal Ore Deposits*; Barnes, H.L., Ed.; Wiley Intersci: New York, NY, USA, 1979; pp. 509–567.

82. Tan, Q.P.; Xia, Y.; Xie, Z.J.; Yan, J. Migration paths and precipitation mechanisms of ore-forming fluids at the Shuiyindong Carlin-type gold deposit, Guizhou, China. *Ore Geol. Rev.* **2015**, *69*, 140–156. [CrossRef]

83. Chang, J.Y. Relationship between Calcite and Metallogenic Process and Prospecting Significance of Zhesang Carlin Type Gold Deposit in Southeast Yunnan. Master's Thesis, Kunming University of Science and Technology, Kunming, China, 2020; pp. 1–80. (In Chinese with English abstract)

84. Xu, B.L.; Tan, Q.P.; Xia, Y.; Zhao, Y.M.; Chen, M.; Wang, Z.P. REE geochemical characteristics and prospecting significance of calcite in Shuiyindong Carlin type gold deposit in Guizhou. *Acta Miner. Sin.* **2020**, *40*, 685–694. (In Chinese with English abstract)

85. Palmer, M.R.; Edmond, J.M. The strontium isotope budget of the modern ocean. *Earth Planet. Sci. Lett.* **1989**, *92*, 11–26. [CrossRef]

86. Veizer, J. Strontium isotopes in seawater through time. *Annu. Rev. Earth Planet. Sci.* **2005**, *17*, 141–167. [CrossRef]

87. Veizer, J.; Compston, W. ^{87}Sr/^{86}Sr composition of seawater during the Phanerozoic. *Geochim. Cosmochim. Acta* **1989**, *38*, 1461–1484. [CrossRef]
88. Yu, S.Y.; Chen, L.M.; Lan, J.B.; He, Y.S.; Chen, Q.; Song, X.Y. Controls of mantle source and condition of melt extraction on generation of the picritic lavas from the Emeishan large igneous province, SW China. *J. Asian Earth Sci.* **2020**, *203*, 1–15. [CrossRef]
89. Gao, J.B.; Yang, R.D.; Chen, J.; Zheng, L.L.; Cheng, W.; Wei, H.R. Multiple proxies indicating methane seepage as the origin of Devonian large barite deposit in Zhenning-Ziyun, Guizhou, SW China. *Ore Geol. Rev.* **2017**, *80*, 18–26. [CrossRef]